



1 **Aqueous OH-initiated photooxidation of smoke extracts from maize**
2 **straw and coal combustion: optical character and molecular**
3 **composition**

4 Zhaolian Ye ^{a,*}, Dandan Hu ^a, Qiuyan Chen^a, Xiangpeng Huang^a, Xinlei Ge^{b,*}

5 ^a School of Resources and Environmental Engineering, Jiangsu University of
6 Technology, Changzhou 213001, China

7 ^b School of Energy and Environment, Southeast University, Nanjing, 211189, China.

8 *Corresponding author, Zhaolian Ye (bess_ye@jsut.edu.cn), xinlei@seu.edu.cn

9

10 **Abstract:** Aqueous-phase •OH photodegradation of coal- and maize-derived
11 smoke extracts was investigated to elucidate their optical and molecular
12 transformations. Parallel factor analysis of excitation-emission matrix fluorescence
13 spectra identified one humic-like and two protein-like substances. FT-ICR MS
14 revealed that CHO (74.5% for maize, 58.9% for coal) and CHON (24.1% for maize,
15 11.8% for coal) compounds dominated both smoke extracts, whereas
16 sulfur-containing species were more abundant in coal smoke (29.4%) than in maize
17 (1.4%). The aqueous •OH photooxidation enhanced molecular saturation and reduced
18 aromaticity, reflected by lower double bond equivalent and aromaticity index values.
19 Lignin-like compounds decreased, whereas lipid- and aliphatic-like fractions
20 increased, indicating transformation of aromatic species into more saturated products.
21 Distinct photodegradation pathways were observed for coal and maize extracts based
22 on changes in resistant, degraded, and newly formed molecules. Reactive species
23 contributed to WSOC degradation in the order •OH > ³C > ¹O₂, with contributions of



24 86.4%, 12.8%, and 0.8% for coal extracts, and 80.9%, 16.0%, and 3.1% for maize
25 extracts, respectively. Increased oxalic acids, CHO_2^+ fragments, and declining pH
26 values during the first 5 h indicated substantial formation of carboxylic acids.
27 Measurements from aerosol mass spectrometry showed increasing oxidation
28 indicators during this early stage, confirming enhanced oxidation of aqueous
29 secondary organic aerosol. Oxidative potential, assessed by dithiothreitol
30 consumption, initially increased and then declined, while its normalization by
31 water-soluble organic carbon increased, likely due to the formation of
32 nitrogen-containing compounds in coal smoke and reactive quinones in maize smoke,
33 respectively. Continued photodegradation led to decreases in light absorption and total
34 fluorescence intensity. Overall, this study improves understanding of aqueous-phase
35 photochemical processing of smoke-derived water-soluble organic matter and
36 supports more accurate representation of these processes in atmospheric models,
37 contributing to better assessments of smoke aging impacts on air quality and climate.

38

39 **Keywords:** molecular transformations, optical characteristic, FT-ICR MS, reactive
40 species, dithiothreitol (DTT) consumption rate

41

42 **1 Introduction**

43 The atmospheric aqueous phase contains a variety of oxidants, such as hydrogen
44 radical ($\cdot\text{OH}$), peroxy radicals, singlet oxygen ($^1\text{O}_2$), and excited triplet states of
45 organic compounds ($^3\text{C}^*$), which can trigger aqueous-phase oxidation reaction.
46 Aqueous-phase process has been recognized as a significant source of secondary



47 organic aerosol (SOA) and key contributors to light-absorbing compounds, thereby
48 influencing radiative forcing and air quality (Arciva et al., 2024; Go et al., 2023).
49 Extensive studies have investigated the chemical composition, light-absorption
50 properties, and SOA mass yield from single-component model compounds (Arciva et
51 al., 2022; Li et al., 2022). Recently, increasing attention has been toward the aqueous
52 photoaging of complex mixtures, including laboratory-generated SOA or
53 multicomponent systems (Gerritz et al., 2024; Go et al., 2024). Moreover, studies on
54 aqueous aging of water-soluble organic matter (WSOM) derived from actual smoke
55 particle or PM_{2.5} extracts provide valuable insights into aqueous-phase processing
56 under more realistic atmospheric conditions (Fan et al., 2018; Hems et al., 2020;
57 Wong et al., 2017). Organic matter (OM) within smoke particles, which accounts for
58 up to 60-90% of total mass, is a complex mixture of aromatic and aliphatic
59 compounds with diverse functional groups. The chemical complexity of these
60 precursors poses challenges for comprehensive product characterization and
61 mechanistic studies. Molecular-level compositional data are therefore crucial for
62 improving our understanding of the role of smoke-derived OM in atmospheric
63 aqueous-phase chemistry. High-resolution mass spectrometry (MS) techniques with
64 soft ionization methods, such as Fourier transform ion cyclotron resonance mass
65 spectrometry (FT-ICR MS), enable detailed molecular characterization in complex
66 mixtures and have been widely applied in aerosol studies (Cao et al., 2025; Wang et
67 al., 2017).

68 To date, only a few studies (Leresche et al., 2021; Lei et al., 2024) have
69 examined photochemical aging characteristics of aqueous extracts of smoke particles
70 or atmospheric fine particulate matter, most of which have appeared only recently.
71 Notably, few investigations have compared the molecular and optical changes during



72 aqueous-phase oxidation of smoke extracts from different fuel sources. Cao et al.
73 (2025) compared molecular-level composition and fluorophore changes of extracted
74 WSOM, but their study did not consider the distinct contributions of various reactive
75 oxygen species (ROS) to the oxidation process. Additionally, the wavelength of the
76 light source can significantly influence the photochemical reactivity of organic
77 compounds. For instance, syringaldehyde was found to inhibit the degradation of
78 vanillyl alcohol under UV-B irradiation due to light-absorbing competition, whereas it
79 promoted the degradation of vanillyl alcohol under UV-A irradiation via the
80 photosensitization effect of syringaldehyde (Li et al., 2024).

81 To elucidate the reaction mechanism involved in aqueous-phase photooxidation,
82 it is crucial to understand the formation, transformation, and roles of ROS during
83 photolysis. Biomass burning smoke—such as that produced from agricultural crop
84 residues—contains a variety of potential organic photosensitizers bearing with
85 carbonyl groups and conjugated double bonds, which can absorb sunlight and
86 generate ROS (e.g., HO_2/O_2^* , $^1\text{O}_2$, $\cdot\text{OH}$), thereby enhancing atmospheric oxidative
87 capacity. However, direct quantification of ROS remains challenging (Gerritz et al.,
88 2024; Leresche et al., 2021; Manfrin et al., 2019). For instance, Gerritz et al. (2024)
89 investigated the photolytic formation of ROS in aqueous extracts of
90 laboratory-generated SOA using an in situ UV-vis irradiation system coupled with
91 electron paramagnetic resonance (EPR) spectroscopy and identified organic peroxides
92 and carbonyls as major ROS precursors. Manfrin et al. (2019) reported the $^1\text{O}_2$
93 formation from photosensitized reactions mediated by aromatic SOA, although free
94 radicals were not directly measured. Due to the chemical complexity of
95 smoke-derived WSOM and the analytical difficulty in quantifying ROS, the
96 underlying reaction mechanisms remain poorly understand.



97 Further investigation into the aqueous photoaging of WSOM from different
98 combustion sources is crucial to understanding the underlying mechanisms driving
99 chemical transformation and light absorption. Comparative studies of maize- and
100 coal-derived WSOM under simulated sunlight can reveal how source-dependent
101 compositions influence photo-reactivity and light-absorbing compounds formation.
102 This study compares the optical, molecular evolution and oxidative potential of maize
103 (a representative agricultural residue) and coal smoke extracts during OH-induced
104 photooxidation. WSOM from both smoke types was analyzed using UV-vis
105 spectrometer, excitation-emission matrix (EEM) fluorescence, and FT-ICR MS to
106 identify similarities and differences in photoaging behavior. High-resolution
107 time-of-flight aerosol mass spectrometers (HR-AMS) were used to characterize the
108 bulk chemical composition of low-volatility organics (denoted as aqSOA) over
109 photoreaction. Our findings will provide insights into the chemical evolution and
110 environmental impacts of smoke-derived organic matter.

111

112 **2 Materials and Methods**

113 **2.1 Chemicals and solutions**

114 The following reagents were purchased from the Sigma-Aldrich
115 (dithiothreitol, >99%; 5,5'-dithiobis (2-nitrobenzoic acid), >99%; benzoic acid, >99%;
116 syringol, >99%; furfuryl alcohol, >99%). Methanol ($\geq 99\%$), acetonitrile ($\geq 99\%$),
117 Na_2CO_3 ($\geq 99\%$) and NaHCO_3 ($\geq 99\%$) were purchased from Acros Chemicals.
118 Sulfuric acid ($\geq 99\%$) was obtained from Sinopharm. $(\text{NH}_4)_2\text{SO}_4$ (GR), H_2O_2
119 (29%~32%) and KOH ($\geq 99\%$) were supplied by Aladdin and Alfa Aesar, respectively.



120 2,2,6,6-Tetramethylpiperidine ($\geq 98\%$) and 5,5-dimethyl-1-pyrroline N-oxide ($\geq 97\%$)
121 were purchased from Anpel Laboratory Technologies (Shanghai) Co., Ltd.

122 All chemicals were used as received without further purification. All solutions
123 were prepared with ultrapure water (resistivity $\geq 18.2 \text{ M}\Omega \text{ cm}$) produced by a Milli-Q
124 purification system.

125 **2.2 Sample collection and experiment preparation**

126 Coal and maize straw were combusted in a self-built stove, which was designed
127 to simulate domestic fuel burning. The schematic of the combustion and sampling
128 systems can be found in our previous publication. Briefly, the stove was connected to
129 a stainless steel dilution tunnel and residence chamber. Smoke particles emitted from
130 maize straw and coal combustion were collected on pre-baked quartz fiber filters
131 ($20.3 \times 25.4 \text{ cm}$, Whatman) using two samplers equipped with cyclone with a $2.5 \mu\text{m}$
132 aerodynamic cutoff.

133 One quarter of each filter was cut into strips and placed in extraction bottles. The
134 samples were ultrasonically extracted three times with 30 mL Milli-Q water. The
135 combined extracts were filtered through a $0.45 \mu\text{m}$ PTFE membrane and subsequently
136 diluted to approximately 15 mgC/L for photoaging experiment based on suggested
137 TOC level ($0.5\text{-}1.4 \text{ mmol C/L}$) by Cook et al. (2017) for cloud water. Photochemical
138 reactions were performed in a Rayonet RPR-200 photoreactor equipped with 14
139 lamps, following the procedure described in detail earlier (Ye et al., 2025). The
140 irradiance intensity on the solution surface was 2.4 mW/cm^2 in the wavelength region
141 of $290\text{-}400 \text{ nm}$ (centered at 313 nm), as measured by a radiometer (Photoelectric
142 Instrument Factory of Everfine Corporation, Hangzhou, China). The intensity is slight



143 lower than natural sunlight levels (6.16 mW/cm²) measured at noon during winter at
144 Jiangsu University of Technology, Changzhou (Wang et al., 2025). Before
145 photooxidation, 10 mM H₂O₂ was added to the reaction solution to generate •OH with
146 certain concentration, consistent with previous study (Arciva et al., 2022; Cao et al.,
147 2025).

148 **2.3 Chemical analysis**

149 Water-soluble organic carbon (WSOC) concentrations were determined using a
150 total organic carbon (TOC) analyzer (TOC-L CPH, Shimadzu, Japan). Metal element
151 concentrations (Fe and Cu) were quantified by inductively coupled plasma-mass
152 spectrometry (ICP-MS, Agilent 7800). Eight water soluble inorganic ions (Na⁺, Cl⁻,
153 SO₄²⁻, NO₃⁻, K⁺, NH₄⁺, Ca²⁺ and Mg²⁺) were also detected for both smoke extracts.
154 Details can be found in Sect. S1 in the Supplement.

155 **2.4 UV-vis and EEM analysis**

156 The UV-vis absorption spectra were monitored using UV-vis spectrophotometer
157 (Shimadzu, Japan) over wavelength range of 200-700 nm. The mass absorption
158 coefficients (MACs, m²/gC), defined as absorbance normalized by WSOC
159 concentration, were calculated as follows:

$$160 \quad MAC_{\lambda} = \frac{A_{\lambda}}{C \times L} \times \ln 10 \quad (1)$$

161 Where A_{λ} represent the absorbance at wavelength λ . C refers to the WSOC
162 concentration of reaction solution. L is the optical path length (1 cm in this study).

163 The EEM spectra were recorded using a three-dimensional fluorescence
164 spectrophotometer (FluoroMax Plus, HORIBA Scientific). Parallel factor analysis



165 (PARAFAC) model was applied to EEM spectra to resolve the fluorescent compounds
166 using the DOMFluor toolbox in MATLAB 2021b. Details of the determination and
167 modeling procedures are provided in our previous study (Ye et al., 2025). Three
168 fluorescence components (C1, C2 and C3) were identified from PARAFAC model.
169 The fluorescence index (FI), humification index (HIX), and biological index (BIX)
170 were further calculated to characterize the fluorescent properties of the samples. The
171 calculation methods for these indicators were shown in the supplement and in our
172 previous study (Ye et al., 2025).

173 **2.5 FT-ICR MS measurement**

174 The molecular compositions, degree of unsaturation, and aromaticity of WSOM
175 were characterized using FT-ICR MS coupled with negative electrospray ionization
176 (ESI). Solid-phase extraction (SPE) was employed for sample pretreatment prior to
177 FT-ICR MS determination, following procedures similar to those described in
178 previous studies (Yang et al., 2025). Briefly, the reaction solution was adjusted to pH
179 2 and pass through SPE cartridges (Oasis HLB, Waters, USA) preconditioned with 15
180 mL methanol and 10 mL Milli-Q water. The retained organic matter was subsequently
181 eluted with 10 mL methanol. The eluate was then concentrated to approximately 0.5
182 mL using a rotary evaporator and stored at -20 °C until analysis. Prior to analysis, the
183 sample was re-dissolved in 4 mL of methanol and filtered through a 0.22 µm PTFE
184 membrane. FR-ICR MS analysis was performed with a capillary voltage of 4.0 kV,
185 and samples were introduced into the ESI source at a flow rate of 120 µL/ h. Mass
186 spectra were acquired over the m/z range of 150 – 800 Da. To improve the
187 signal-to-noise ratio and dynamic range, each spectrum was averaged from 200 scans.
188 Blank samples were analyzed under the same procedure. Notably, no water-insoluble



189 precipitates larger than 0.22 μm were observed during photooxidation. However,
190 filtration of the reaction solution through a 0.22 μm membrane prior to analysis may
191 resulted in the loss of some newly formed oligomers.

192 The Composer software (Sierra Analytics, USA) was utilized to process the
193 FT-ICR MS spectra and assign elemental compositions to recalibrated peaks, with a
194 mass tolerance of ± 1.0 ppm and a signal-to-noise ratio (S/N) threshold of ≥ 4 . Based
195 on the assigned molecular formulas, WSOM compounds were categorized into four
196 groups: CHO, CHON, CHOS, and CHONS. To evaluate the degree of unsaturation
197 and aromaticity, double bond equivalent (DBE) and aromaticity index (AI) were
198 calculated as follows:

$$199 \quad \text{DBE} = \frac{1}{2} \times (2c + 2 - h + n) \quad (2)$$

$$200 \quad \text{AI} = \frac{1 + c - 0.5o - s - 0.5h}{c - 0.5o - s - n} \quad (3)$$

201 The intensity-weighted averaged characteristic parameters can be expressed as:

$$202 \quad P_w = (\sum P_i \times I_i) / \sum I_i \quad (4)$$

203 where P represents DBE, AI, molecular weight (MW), oxygen-to-carbon (O/C) or
204 hydrogen-to-carbon (H/C) ratio. P_i represents the corresponding parameter value for
205 each individual compound I , and I_i represents the relative abundance of its molecular
206 formula.

207 Molecular formulas were further classified into seven compound classes based
208 on their H/C and O/C ratios (Ning et al., 2025): lipid-like ($1.5 < \text{H/C} \leq 2.0$, $0 \leq \text{O/C} \leq 0.3$);
209 aliphatic -like ($1.5 < \text{H/C} \leq 2.2$, $0.3 < \text{O/C} \leq 0.67$); lignin-like ($0.67 < \text{H/C} \leq 1.5$, $0.1 \leq$
210 $\text{O/C} < 0.67$); carbohydrate-like ($1.5 < \text{H/C} \leq 2.5$, $0.67 < \text{O/C} < 1.2$); unsaturated



211 hydrocarbon-like ($0.67 < H/C \leq 1.5$, $O/C < 0.1$); condensated aromatic-like ($0.2 \leq H/C$
212 ≤ 0.67 , $O/C < 0.67$), and tannin- ($0.6 < H/C \leq 1.5$, $0.67 \leq O/C \leq 1.2$). The saturated
213 compounds were defined as the sum of lipid-like and aliphatic components.

214 2.6 HR-AMS analysis of aqSOA composition and mass yield

215 High-resolution aerosol mass spectrometer (HR-AMS, Aerodyne Res. Inc.) was
216 used to characterize the bulk chemical composition of aqSOA, including average
217 elemental ratios (i.e., oxygen-to-carbon ratio (O/C) and hydrogen-to-carbon ratio
218 (H/C)) and some specific fragment ions. The average oxidation state of carbon (OSc =
219 $2 \times O/C - H/C$) was used to index the oxidation degree of aqSOA. 10 mg/L ammonium
220 sulfate was added into the solution as an internal standard for quantifying SOA mass
221 concentration. The aqSOA mass yield was calculated as follows:

222

$$223 \quad \text{SOA yield} = \frac{[Org]_t - [Org]_0}{[WSOC]_0 - [WSOC]_t} = \frac{[Org]_t \times \frac{[SO_4^{2-}]_t}{[SO_4^{2-}]_{AMS}^t} - [Org]_0 \times \frac{[SO_4^{2-}]_0}{[SO_4^{2-}]_{AMS}^0}}{([WSOC]_0 - [WSOC]_t) \times M/12} \quad (5)$$

224

225 Where $[SO_4^{2-}]_t$ and $[SO_4^{2-}]_0$ denote sulfate concentrations (mg/L) in the solution at
226 irradiation time t and zero, respectively. Here, $[SO_4^{2-}]_t$ was equal to $[SO_4^{2-}]_0$ assuming
227 sulfate was not loss during irradiation. The $[Org]$ and $[SO_4^{2-}]_{AMS}$ denote the apparent
228 concentrations of aqSOA and sulfate measured by AMS. $[WSOC]_t$ and $[WSOC]_0$ was
229 WSOC concentration in the solution measured by TOC at irradiation time t and zero,
230 respectively. M represents the averaged molecular weight of mixed solution which
231 can be estimated by FT-ICR MS.

232 3 Results and discussion



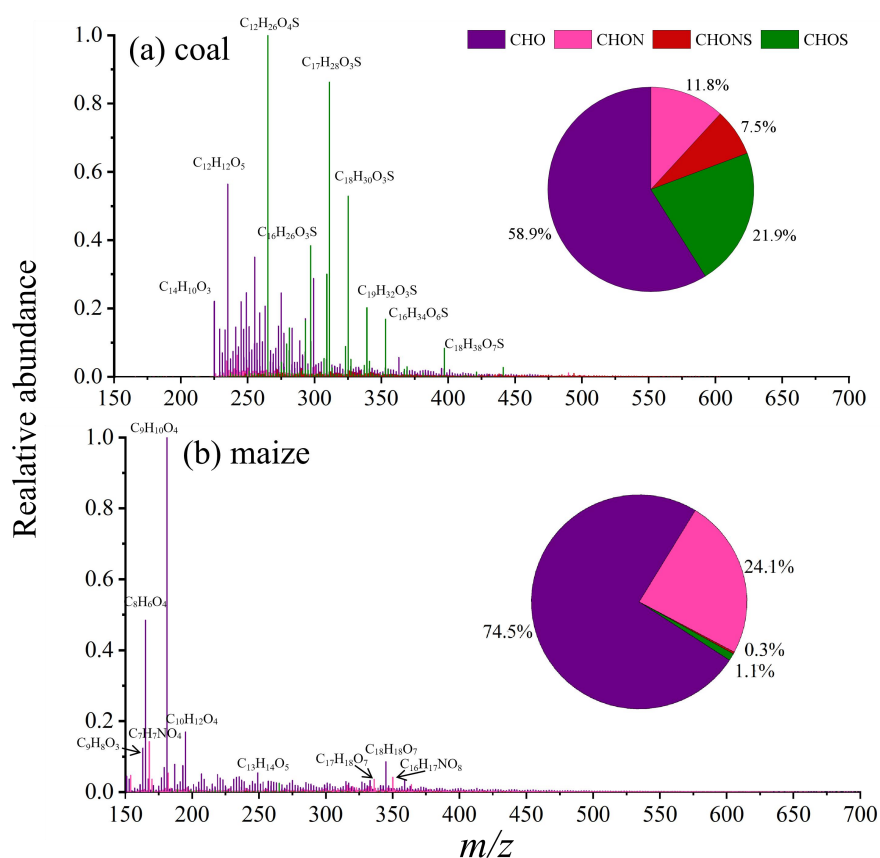
233 3.1 Overall characteristics of smoke extracts

234 Fig. 1 showed the reconstructed FT-ICR mass spectra of WSOM for two fresh
235 extracts samples. Based on the intensity of each negative ion, the average molecular
236 formulas for coal and maize smoke extracts calculated as $C_{18.0}H_{24.0}O_{6.9}N_{0.90}S_{0.41}$ and
237 $C_{21.0}H_{21.7}O_{7.4}N_{0.86}S_{0.04}$, respectively, showing higher C in maize smoke extracts,
238 consistent with previous finding (Fan et al., 2016). In this study, these identified
239 molecular formulas were classified into four main compound groups based on their
240 compositions: CHO, CHON, CHOS, and CHONS. The relative abundances of the
241 four groups were determined by normalizing the magnitude of each peak to the total
242 magnitude of all identified peaks. Most peaks were located within the m/z range of
243 200–400. The greatest peak magnitudes were mainly distributed within the m/z range
244 of 250–350. Distinct peak distribution patterns were observed for both smoke extracts.
245 For example, several CHOS compounds with high relative abundance, such as
246 $C_{12}H_{26}O_4S$, $C_{17}H_{28}O_3S$, $C_{18}H_{30}O_3S$, were identified in the coal smoke extract, whereas
247 the high-abundance CHO and CHON compounds, including $C_8H_{10}O_4$, $C_7H_7NO_4$, and
248 $C_{18}H_{18}O_7$ were predominant in the maize smoke extract. It should be noted that peak
249 magnitude is not indicative of a compound's concentration in a sample due to inherent
250 biases of C18 extractions and electrospray ionization efficiencies.

251 To better illustrate the differences in the \bullet OH oxidation behavior between the
252 two extracts, the concentrations of inorganic ions and transition metals (Fe and Cu) in
253 the fresh WSOM were also measured, as shown in Table S1. It can be seen that the
254 concentrations of Cl^- and NH_4^+ ions in maize were much higher than those in coal,



255 whereas the concentration of SO_4^{2-} ions in coal was higher than that in maize. During
256 the photochemical reaction, the concentrations of these ions showed little change. In
257 addition, the concentrations of Fe and Cu ions were very low, almost below the
258 detection limits of the instrument. These results indicate that the influence of ions on
259 the photochemical reaction can be neglected, especially that of Fe and Cu.



260

261 **Fig. 1.** Reconstructed ESI FT-ICR mass spectra of (a) coal and (b) maize smoke extracts colored

262 by formula groups. The inserted pie charts show the percentage of four formula groups by

263 intensity.

264



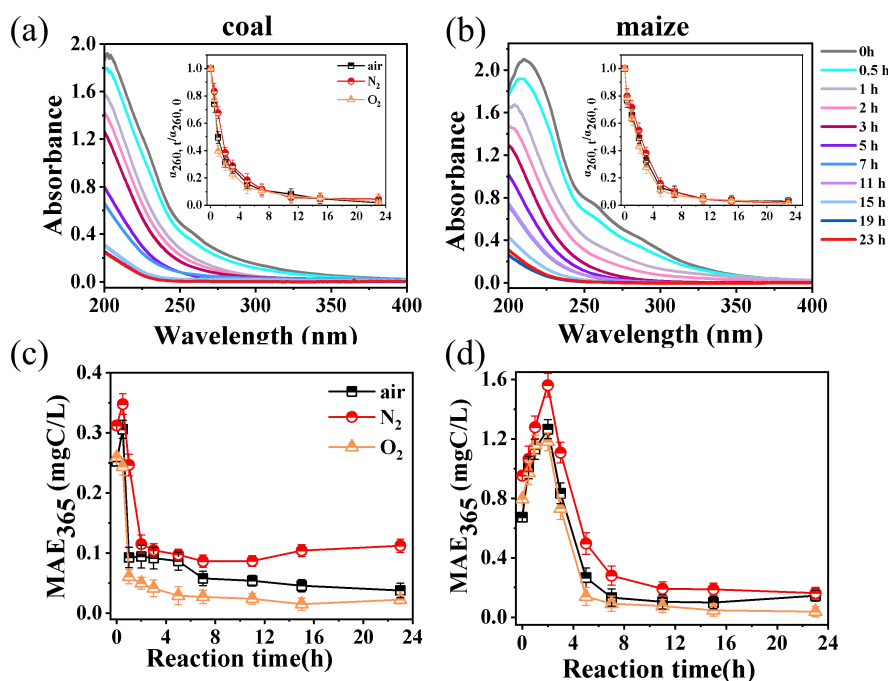
265 **3.2 Optical properties of smoke extracts photooxidation**

266 **3.2.1 Absorbance characteristics**

267 Aqueous \bullet OH oxidation of two extracts—involving both photolysis and ROS
268 oxidation reactions—can markedly alter their optical properties by degrading existing
269 chromophores or generating new light-absorbing compounds. Fig.2 (a, b) shows the
270 UV-vis absorbance spectra in the range of 200-500 nm of the reaction solutions at
271 varying irradiation time. Although the spectra were generally broad and featureless,
272 noticeable differences in the absorption intensity were observed between coal and
273 maize smoke. A distinct shoulder at 260 nm was observed in the spectra of maize
274 smoke WSOM, attributed to π - π^* transitions of unsaturated double bonds (e.g., C=C
275 and C=O) (Li et al., 2021), indicating the presence of fulvic acid-like chromophores.
276 As the reaction progressed, overall decreases in absorbance (Fig. 2) were observed for
277 both types of smoke extracts, which can be ascribed to the degradation of compounds
278 containing carbonyl- and double bond groups. Tomaz et al. (2018) similarly reported
279 that aqueous \bullet OH oxidation of complex BB mixtures led to rapid depletion of
280 phenolic compounds and formation of small organic acids. Consistent with these
281 findings, photobleaching (i.e. decrease in light absorbance) is the most common effect
282 observed upon irradiation of SOA or BrC in the aqueous phase (Jiang et al., 2023).
283 The decreased light absorption was likely due to competing processes, including the
284 formation of light-absorbing products and fragmentation yielding less absorptive
285 compounds. The study by Chen et al. (2025) on molecular structure-dependent light
286 absorption demonstrated that CHO compounds with low molecular weight and high



287 aromaticity are primarily responsible for absorption in the 200–300 nm range,
288 whereas CHON compounds (mainly nitroaromatics) and highly aliphatic structures
289 play a dominant role in absorption above 365 nm. However, the present results differ
290 from recent studies on aqueous SOA formation from the photooxidation of coal and
291 rice straw burning WSOM, which reported photoenhancement at wavelength above
292 360 nm (Cao et al., 2025). Such discrepancies may be attributed to differences in light
293 sources, OH concentrations, and the molecular composition of the smoke extracts.
294 Clearly, different classes of compounds in smoke extracts exhibit distinct
295 photochemical aging behavior, including photoenhancement, photobleaching or a
296 combination of both.



297

298 **Fig. 2.** (a, b) The UV-vis absorption spectra under different irradiation time for coal and maize
299 smoke extracts, and (c, d) MAE at 365 nm over photoaging time. The inset shows the change in



300 absorbance at the wavelength of 260 nm compared to the spectra at time = 0.

301

302 Changes in MAC_{365} are commonly used to track chromophore evolution since
303 different chromophores exhibit varying light-absorbing ability. Fig. 2(c, d) shows the
304 variation of the MAC_{365} over reaction time for both smoke extracts. For both smoke
305 extracts, MAE_{365} initially increased and then declined. The enhancement in
306 light-absorbing can be mainly ascribed to two factors (Jiang et al., 2021). First,
307 OH-addition to aromatic rings produces OH-rich compounds that act as chromophores
308 (Lei et al., 2024). Second, the formation of dimers and larger oligomers extends
309 π -conjugation, shifting absorption to longer wavelengths and enhancing light
310 absorption. Generally, increased functionalization and oligomerization increased light
311 absorption (Go et al., 2024; Vione et al., 2019). As the reaction proceeds, these
312 intermediate chromophores transform into smaller, ring-opened molecules with
313 weaker or negligible light absorption. The aqueous-phase photoaging of phenolic
314 SOA also showed that light-absorbing properties of oxidation products were strongly
315 time-dependent (Jiang et al., 2023). Additionally, photodegradation of WSOM can
316 generate more volatile products, and their evaporation may reduce WSOC (Fig. S1),
317 thereby influencing the light absorption per unit C mass. The final decrease in
318 MAE_{365} can be supported by the FT-ICR MS results (Sect. 3.3), which show
319 reductions in lignin and aromatic compounds and increase in aliphatic species,
320 accompanied by enhanced protein-like fluorescence (Sect. 3.2.2). Another spectral
321 parameter, $E2/E3$ (the ratio of absorbance at 250 nm to that at 365 nm), further



322 characterizes these changes. During the first hour of $\cdot\text{OH}$ oxidation, E2/E3 decreased
323 from 16 to 8 for coal smoke, indicating enrichment in high-molecular-weight
324 chromophores with stronger light-absorbing capability. However, it increased from 12
325 to 22 for maize smoke extracts (Fig. S2). These contrasting E2/E3 trends highlight
326 distinct molecular transformations in WSOM for coal and maize smoke under $\cdot\text{OH}$
327 oxidation.

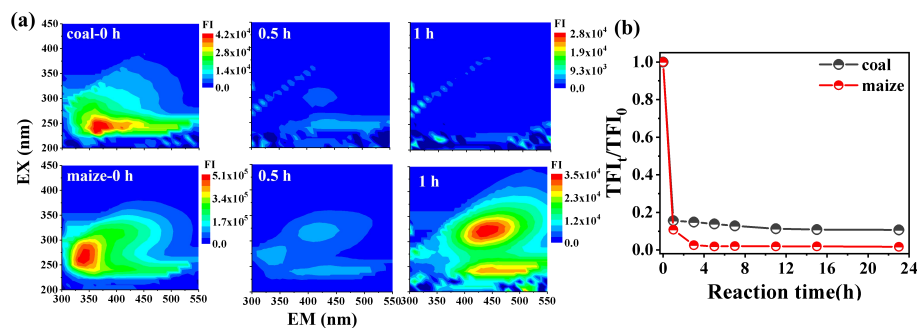
328 **3.2.2 Fluorescence properties**

329 Fluorescence spectra provide more detailed molecular information than UV-vis
330 spectra. For example, a red shift in the excitation–emission maximum typically
331 indicates increased aromaticity and higher molecular weight (Tang et al., 2020). Fig.
332 3a presents the EEM spectra of both smoke samples upon irradiation. We clearly
333 observed that the intensity of the characteristic fluorescence peak at Ex/Em=275/350
334 nm kept decreasing within the first hour of the reaction, while two new fluorescence
335 peaks appeared at Ex/Em=325/400-500 nm and Ex/Em=225/400-500 nm, indicating
336 the formation of humic-like chromophores. However, as the reaction proceeded, the
337 intensity of these new peaks gradually weakened. The Hulis-C concentration also
338 increased at the first 1-3 h for both smoke extracts and then decreased over time (Fig.
339 S3). As seen in Fig. 3b, total fluorescence intensity (Ex=250-450 nm, Em=300-650
340 nm) decreased quickly at the first hour and then decreased more slowly.

341 The HIX, BIX and FI were further employed to evaluate the degree of
342 humification and freshness of organic matters. As suggested by Wu et al. (2021), an
343 increase in HIX accompanied by decrease in BIX and FI can serve as indicators of



344 enhanced oxidation of atmospheric WSOC. As shown in Fig. S4, the HIX value
345 increased during the first hour and then decreased, suggesting that the formation of
346 humic-like substances initially exceeded their subsequent degradation. Conversely, FI
347 and BIX values decreased at the early stage of oxidation for both smoke samples (Fig.
348 S4). In general, greater humification is associated with lower protein content,
349 primarily due to a reduction in carbon-hydrogen compounds and a red shift in the
350 fluorescence emission wavelength of more humified molecules. Conversely, a higher
351 BIX indicates a higher contribution from protein-like and amino acid components.



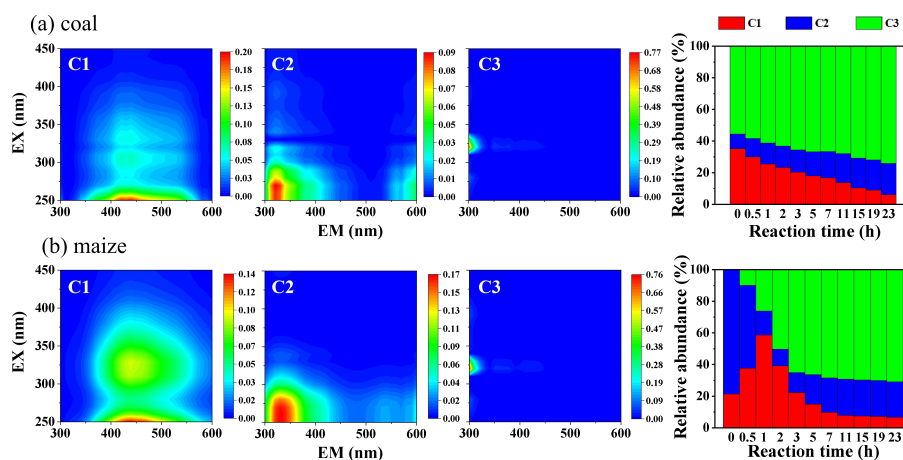
352 **Fig. 3.** (a) Variation trend of EEM fluorescence spectra and (b) temporal profiles of total
353 fluorescence intensity for two smoke extracts.
354

355
356 The PARAFAC model identified three underlying fluorescent components,
357 including one humic-like components (C1) and two protein-like component (C2 and
358 C3) (Fig. 3). Component C1 is considered to be a humic-related substance,
359 characterized by two peaks at Ex/ Em=230/400–500 nm and 300/400-500 nm (Huang
360 et al., 2025). C2 displays peaks at Ex/Em=250-300/300-350 nm, which can be
361 attributed to tyrosine-like components. C3 (Ex/Em=325/300 nm) is likely link to



362 tryptophan-like components. As shown in Fig. 4, the proportion of C1-C3 in both
363 maize and coal WSOM varied dynamically throughout photochemical processes. For
364 coal WSOM, C1 fraction decreased, whereas C2 and C3 increased. In contrast, for
365 maize WSOM, C2 gradually transformed into C1 at the first hour, resulting in
366 opposite trends between the two components. This transformation likely reflects the
367 formation of more oxygenated humic-like substances via OH-functionalization at the
368 early stage, consistent with change trends of Hulis-C for maize smoke extracts (Fig.
369 S3). This interpretation can be further confirmed by the increase in HIX values for
370 maize smoke during the first hour of photooxidation (Fig. S4 c).

371 For both smoke WSOM samples, the C3 component exhibited a gradual increase
372 over time. The findings are in accordance with other's study on the photooxidation of
373 WSOC emitted from rice straw combustion (Zhang et al., 2021). The stronger
374 fluorescence intensity observed at Ex/Em=325/300 nm may correspond to low-ring
375 PAHs and their derivatives, which are known to be produced in abundance during
376 biomass pyrolysis or burning (Mahamuni et al., 2020). Overall, the EEM components
377 varied depending on the types of smoke-derived WSOM.



378



379 **Fig. 4.** Three fluorescent components (C1-C3) of the smoke extracts identified by the
380 EEM-PARAFAC model and variations in the relative contributions of each PARAFAC
381 component of (a) coal and (b) maize smoke extracts with photoaging time.

382

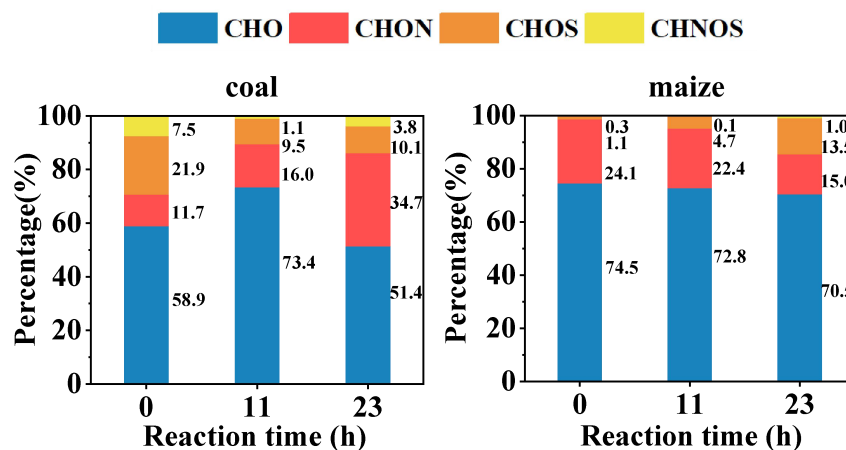
383 **3.3 Molecular composition of WSOM via FT-ICR MS**

384 The intensity weighted average values of various molecular
385 parameters—including molecular weight (MW), elemental ratios (H/C and O/C), DBE,
386 AI—for maize and coal smoke extracts before and after photoaging were summarized
387 in Table 1. As listed in Table 1, a total number of 5596 and 5107 molecular formulas
388 were identified for fresh coal and maize extracts, respectively, within the m/z range of
389 100-600, indicating the complicated molecular compositions of WSOM. For coal
390 WSOM, the MW decreased slightly 313 g/mol in the fresh sample to 296 and 288
391 after 11 h and 23 h photooxidation, respectively. The MW for maize remained nearly
392 unchanged during OH-photooxidation.

393 The dominant species in both smoke extracts were CHO and CHON compounds,
394 with higher abundance observed in maize than in coal smoke extract (Fig. 5).
395 Molecular composition analysis further revealed that maize smoke WSOM was
396 largely composed of CHO and CHON, together accounting for 98.6% of the total
397 peak area. CHO compounds constituted more than half of all identified molecular
398 formulas in both WSOM samples (74.5% for maize and 58.9% for coal). In contrast,
399 S-containing compounds (CHOS and CHONS) were much more abundant in coal
400 smoke extracts (29.4% in total) than in maize (1.4% in total). Similarly, previous
401 studies reported that the fractions of S-containing CHOS and CHONS species in



402 crop-derived WSOM were relatively low (3-9% in peak area) (Li et al., 2024).
403 Interestingly, S-containing compounds in coal smoke decreased by nearly 50% after
404 photodegradation, whereas their abundance increased markedly in maize smoke
405 extracts. Meanwhile, the proportion of CHON compounds in coal smoke increased,
406 indicating the gradual formation of N-containing oxidation products during aging.
407 Conversely, the CHON proportion in maize smoke decreases with irradiation time,
408 likely due to the progressive degradation of nitroaromatic compounds commonly
409 present in biomass burning emissions.



410
411 **Fig. 5.** Change of relative abundance fraction of four groups (CHO, CHON, CHOS, and CHONS)
412 with reaction time in both smoke extracts.

413 The molecular-level parameters are summarized in Table 1. The DBE values
414 ranged from 2 to 9 for coal smoke extracts and from 2 to 11 for maize smoke extracts.
415 The unsaturation and aromaticity of molecular formulas can be evaluated using the
416 H/C ratios and the DBE values, where lower H/C and higher DBE indicate greater
417 unsaturation and, to some extent, aromatic character. As presented in Table 1, aged



418 WSOM were characterized by higher H/C values (1.75 vs 1.32 for coal, and 1.68 vs.
419 1.02 for maize), lower DBE values (3.85 vs. 7.12 for coal, and 4.08 vs. 8.99 for
420 maize), and reduced AI values (0.16 vs. 0.31 for coal, and 0.16 vs. 0.48 for maize)
421 after 23 h of photooxidation compared to the fresh samples. These variations in AI,
422 DBE and H/C suggest the breakdown of aromatic structure and an overall
423 enhancement in molecular saturation. This observation is consistent with the findings
424 from dark aqueous \bullet OH oxidation of BB smoke WSOC reported by Fan et al. (2024).
425 Moreover, the aromaticity of CHON compounds markedly decreased, as indicated by
426 their lower AI and DBE values (Table 1), leading to reduced light absorbance. The
427 number and intensity of CHON compounds increased after OH photooxidation, which
428 might be attributed to oxidation of reduced N-containing species (i.e., CHN^+ ,
429 CHON^+).

430 Additionally, the O/C increased from 0.38 to 0.45 for coal and from 0.40 to 0.55
431 after 11 h of oxidation, followed by a decrease to 0.27 and 0.25 at 23 h, respectively.
432 This trend indicates a transformation from OH-functionalization to fragmentation as
433 photooxidation progressed. A decrease in DBE per carbon (DBD/C) was observed
434 after 23 h of photodegradation—from 0.45 to 0.25 for coal and 0.62 to 0.27 for
435 maize—further confirming the transformation of refractory aromatic-condensed
436 structures into more polar and readily degradable small molecules. Fig. S5 shows the
437 relationship between DBE values and C atom numbers for four compound groups
438 identified by FT-ICR MS.

439 **Table 1** Intensity-weighted average molecular parameters (MW, elemental ratios, DBE, DBE/C,
440 AI) of coal and maize smoke WSOM before and after OH photooxidation



Sample	Time	Elemental composition	Formulas number	MW (g/mol)	DBE	AI	O/C	H/C	DBE/C
coal	0 h	Total	5596	312.98	7.12	0.31	0.38	1.32	0.45
		CHO	1728	300.23	8.16	0.38	0.36	1.16	0.52
		CHON	1695	323.12	8.77	0.43	0.49	1.25	0.54
		CHOS	702	310.03	3.60	0.10	0.31	1.74	0.23
		CHONS	1471	406.27	6.61	0.19	0.55	1.48	0.41
	11 h	Total	5157	296.35	4.58	0.17	0.45	1.57	0.34
		CHO	2066	286.35	4.61	0.16	0.47	1.54	0.35
		CHON	2029	312.31	4.10	0.16	0.40	1.68	0.31
		CHOS	816	343.04	4.93	0.16	0.29	1.62	0.29
		CHONS	246	329.73	6.45	1.01	0.86	1.63	0.54
	23 h	Total	5072	288.32	3.85	0.16	0.27	1.75	0.25
		CHO	1348	262.69	4.04	0.15	0.26	1.66	0.28
		CHON	1970	304.36	2.03	0.07	0.25	1.99	0.14
		CHOS	723	313.19	4.80	0.17	0.31	1.67	0.27
		CHONS	1031	398.63	7.04	0.33	0.52	1.63	0.39
maize	0 h	Total	5107	286.90	8.99	0.48	0.40	1.02	0.62
		CHO	2143	273.62	8.56	0.46	0.40	1.02	0.61
		CHON	2772	329.45	10.52	0.54	0.40	0.98	0.66
		CHOS	107	248.21	4.61	0.22	0.46	1.37	0.47
		CHONS	85	317.32	7.31	0.28	0.56	1.13	0.61



	Total	6027	288.84	5.44	0.21	0.55	1.40	0.44
	CHO	2643	283.95	5.19	0.19	0.56	1.41	0.42
11 h	CHON	2954	301.07	6.59	0.30	0.57	1.29	0.54
	CHOS	395	305.41	3.69	0.12	0.35	1.83	0.20
	CHONS	35	317.42	10.37	0.45	0.23	1.19	0.54
	Total	5147	285.81	4.08	0.16	0.25	1.68	0.27
	CHO	2647	277.01	4.20	0.16	0.23	1.65	0.27
23 h	CHON	1995	296.44	4.14	0.19	0.28	1.69	0.30
	CHOS	400	312.24	2.94	0.09	0.34	1.86	0.18
	CHONS	105	393.70	10.63	1.03	0.49	1.11	0.67

441

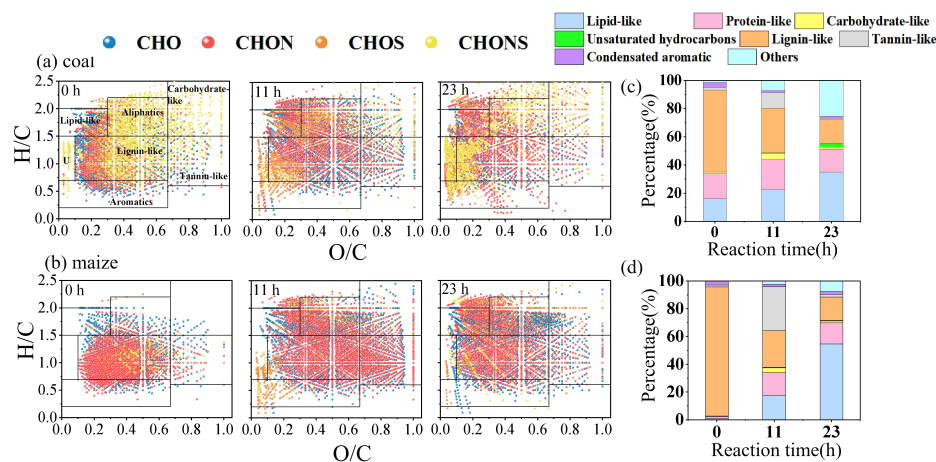
442 The van Krevelen diagram (Fig. 6), which plots the O/C ratio as the x-axis and
443 the H/C ratio on the y-axis, was used to elucidate the molecular distribution. For
444 clarity, the corresponding detailed values were listed in Table S2. Lignin-like
445 compounds dominated both coal and maize smoke WSOM, accounting for 58.2% and
446 93.1% of total intensity, respectively, indicating a greater abundance of phenolic
447 organic species in maize smoke. Previous study also showed that CHO formulas were
448 mainly lignin-pyrolysis products (Song et al., 2018). After photoaging, the lignin-like
449 fraction decreased significantly, reflecting the degradation of aromatic phenolic
450 species. Given that most lignin-like compounds possess strong light-absorbing
451 properties, their decomposition directly contributed to the observed decrease in
452 absorbance. In contrast, the intensity of saturated compounds (sum of lipids and
453 aliphatic components) increased substantially after OH-induced photooxidation, from
454 33.8 % to 51.2% at 23 h for coal and from 2.4% to 69.8 % for maize. These



455 observations suggest a significant increase in saturated aliphatic and O-enriched
456 compounds (e.g., –OH, –COOH) after OH photooxidation.

457 In addition, the initial increase followed by a decrease (from 11.2% to 1.1% for
458 coal and 31.8% to 2.1% for maize smoke) in tannin-like compounds suggests that
459 radical coupling, condensation, or addition reactions likely occurred during the early
460 stage of the reaction, leading to a higher O/C ratio at 11 h compared to the fresh
461 sample.

462 Condensed aromatic molecules, characterized by low H/C and O/C ratios but
463 high AI, showed a slight decrease with photoaging, indicating the partial degradation
464 of highly aromatic structures. Overall, the reduction in aromatic and lignin-like
465 compounds aligns with the observed decline in the light-absorbing properties (see
466 Sect. 3.2.1). In all, aromatic and lignin-like compounds were continuously
467 transformed into lipid- and aliphatic-like compounds. During the initial stage (first 5
468 h), carbohydrate-like substance such as oxalate were generated (Fig. S6), but their
469 abundance subsequently decreased, consistent with the pH variation that first declined
470 (initial 3 h) and then increased again (Fig. S7). The formation of carboxylic acids can
471 be further confirmed later by identifying their characteristic fragment ions using
472 HR-AMS.



473

474 **Fig. 6.** (a, b) Van Krevelen diagrams of four groups (CHO, CHNO, CHOS, and CHONS) and (c,d)

475 Intensity-weighted fractions of seven major molecular classes. Saturated compounds represent the
476 sum of lipid-like and aliphatic components. U represents unsaturated hydrocarbons.

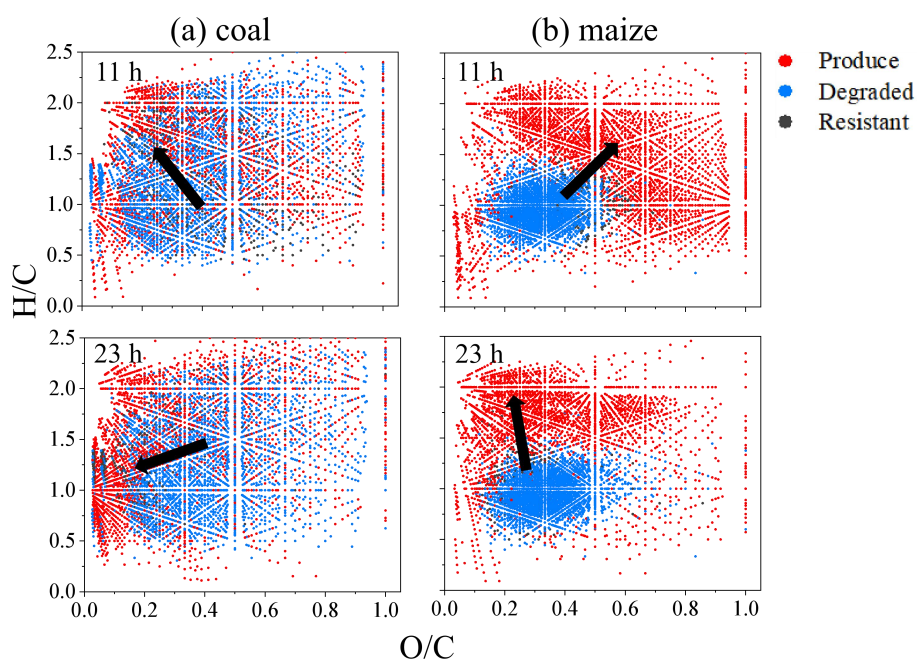
477

478 To further elucidate the photooxidation behaviors of both smoke extracts, the
479 number proportions of resistant, degraded and newly produced molecules were
480 summarized in Table S3. After 11 h of irradiation, 55.1 % and 58.2% of the total
481 formulas in fresh coal and maize, were degraded, resulting in 51.3% and 64.6% newly
482 formed formulas. From 11 h to 23 h, the numbers of newly produced and degraded
483 molecules increased slightly for coal but decreased for maize. Fig. 7 illustrates the
484 O/C vs. H/C distributions of degraded and newly formed compounds after 11 h and 23
485 h of photodegradation. For coal, most degraded compounds were located in high O/C
486 regions, whereas some newly formed species with much lower O/C and higher H/C
487 were likely associated with unsaturated hydrocarbons and lipid-like species. In
488 contrast, maize exhibited a marked shift from low to high O/C and H/C compounds at



489 11 h, resulting in an increase in average O/C ratio. This trend suggests that maize
490 compounds mainly underwent functionalization during the first stage—introducing
491 oxygen-containing groups without breaking the carbon skeleton, thereby increasing
492 O/C and slightly lowering or maintaining H/C. Overall, these results reveal distinct
493 degradation pathways and product characteristics for coal and maize smoke extracts.

494



495

496 **Fig. 7.** Van Krevelen diagrams of resistant, degraded and produced formulas in WSOM derived
497 from (a) coal and (b) maize burning before and after OH photooxidation.

498 3.4 AqSOA composition and mass yield

499 The aqSOA spectra exhibited higher mass fractions of $C_xH_y^+$ and $C_xH_yO_1^+$
500 ions but lower fractions of $C_xH_yN_p^+$ and $C_xH_yO_xN_p^+$ ions (Fig. 8). For corn-derived
501 aqSOA, the fractions of $C_xH_y^+$ and $C_xH_yO_1^+$ both decreased by approximately 10%



502 with increasing photolysis time, while $C_xH_yO_2^+$ increased substantially from 15.95%
503 to 29.96% after 23 h of photoreaction. In contrast, for coal-derived aqSOA, the
504 fraction of $C_xH_yO_1^+$ increased with irradiation time, while no corresponding increase
505 in $C_xH_yO_2^+$ was observed. This suggests that the overall oxidation degree of
506 coal-derived aqSOA did not increase significantly relative to that prior to irradiation.

507 Table S4 summarizes the chemical properties, mass concentration and yield of the
508 formed aqSOA and their evolution during the photoreaction. Both f_{44} and OSc values
509 increased during the first 5 -7h of photoreaction, indicating an enhanced degree of
510 oxidation of aqSOA at the initial stage of the photochemical processing for both
511 samples. However, as the photoreactions progressed, the H/C ratio shows only
512 minimal variation. Our observations also suggested that maize aqSOA becomes
513 increasingly more oxidized during the first stage due to functionalization reactions
514 compared to coal, then decreasing degree of oxidation slightly as a result of
515 fragmentation. Notably, the significantly higher O/C ratios and OSc of maize-derived
516 aqSOA compared to those of the precursors suggest that aqueous-phase processing
517 can serve as an effective source of oxygenated SOA in regions influenced by biomass
518 burning emissions. The value of f_{43} remained relatively low value (less than 0.1) and
519 is therefore not discussed further.

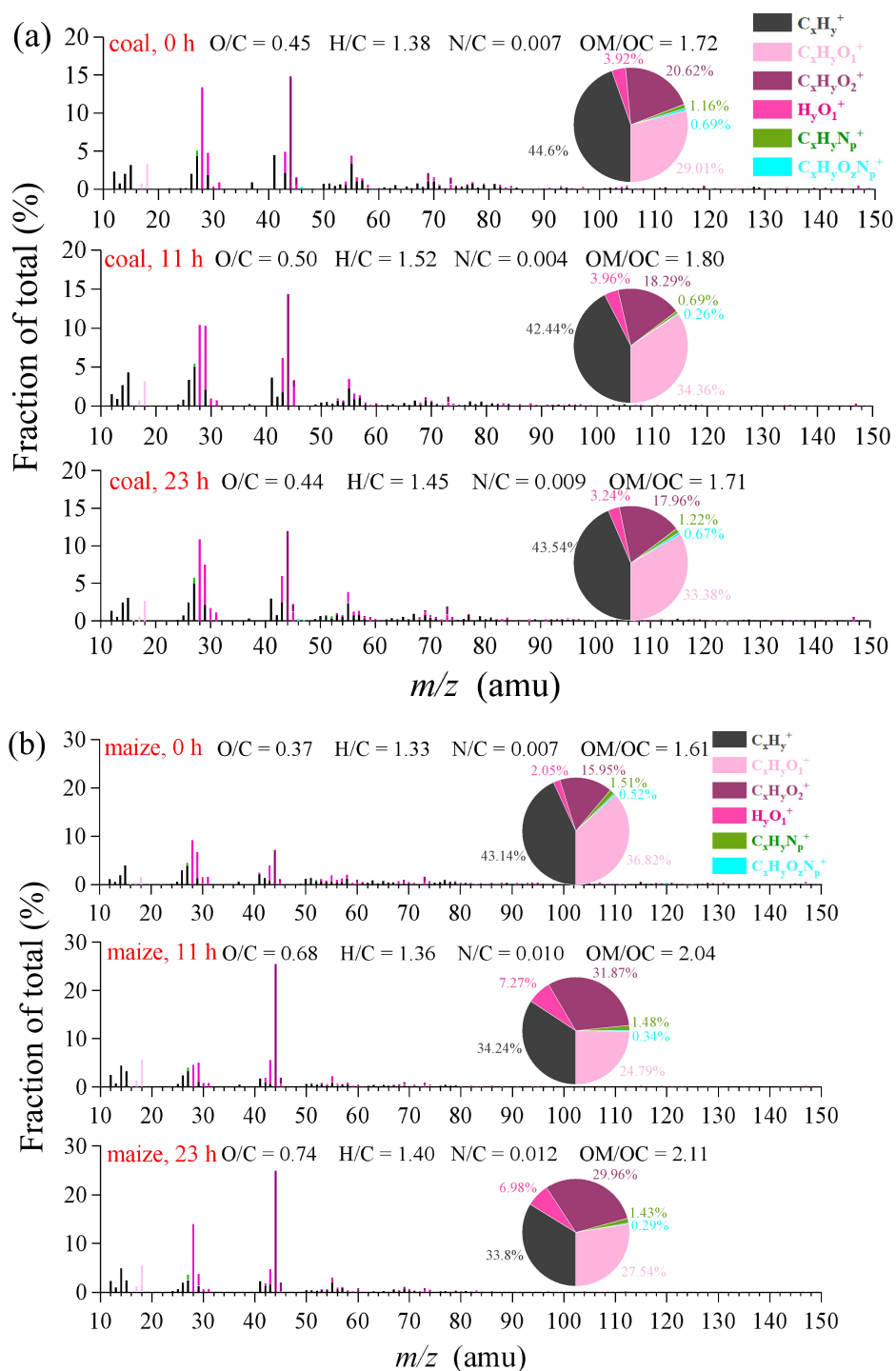
520 For coal samples, the aqSOA mass concentration ranged from 50.77 mg/L to
521 126.95 mg/L. It reached a minimum at 11 h and subsequently increased to 126.95
522 mg/L at 23 h. Correspondingly, the aqSOA mass yield peaked at 148.44% at 1 h,
523 continuously decreased to 1.87% within 9 h, and then increased again to 33.91% at 23



524 h. The aqSOA mass yield of maize was significantly lower (less than 10%) than that
525 of coal samples, indicating that coal sample is more efficient at generating
526 low-volatility species compared to maize.

527 The significant formation of carboxylic acids during the first 9 h of photoreaction
528 is further evidenced by the Van Krevelen diagram (H/C versus O/C), in which aqSOA
529 evolves along a slope of approximately -1 throughout the photooxidation process (Fig.
530 S8). Consistently, the CHO_2^+ ion in the aqSOA AMS spectra—commonly used as a
531 tracer for carboxylic functional groups—exhibits a continuous increase during the
532 first 5 h of photoreaction (Fig. S9). After 3–9 h of reaction, the concentration of
533 CHO_2^+ decreases, accompanied by a decline in f_{44} . A plausible explanation is the
534 occurrence of fragmentation reactions, during which the oxidation products initially
535 formed through oligomerization or functionalization decompose into smaller, more
536 oxidized species. This trend has also been reported in previous studies on the
537 photooxidation of phenolic carbonyls (Jiang et al., 2021).

538



539

540

541 **Fig. 8.** High-resolution MS profiles for aqSOA products at 0 h, 11h and 23h for (a) coal and (b)



542 maize. The peaks in the mass spectra are color-coded according to six ion categories: $C_xH_y^+$,
543 $C_xH_yO_1^+$, $C_xH_yO_2^+$, $H_yO_1^+$, $C_xH_yN_p^+$ and $C_xH_yO_xN_p^+$ ions. The inserted pie charts denote the mass
544 fraction of each ion family to the total MS.

545

546 **3.5 DTT analysis**

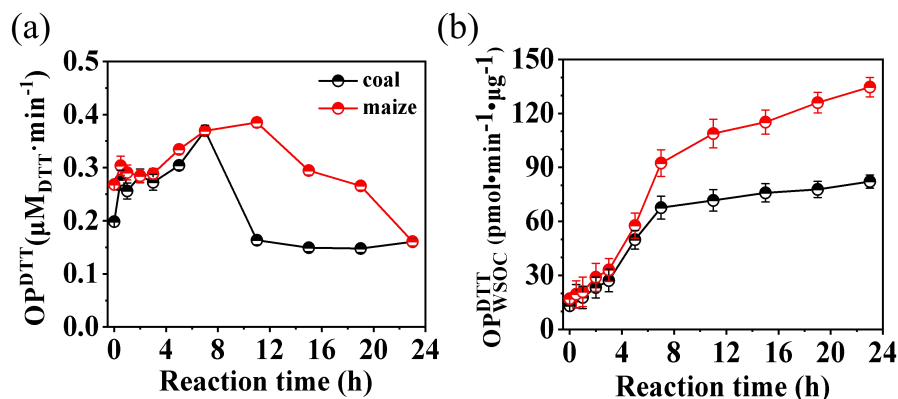
547 Aqueous photochemical aging of BB smoke can also alter its toxicity. The
548 oxidative potential of the reaction solutions was evaluated using the dithiothreitol
549 (DTT) assay, as described in our previous work (Ye et al., 2025). As shown in Fig. 9a,
550 based on the DTT consumption rate (OP^{DTT}), OH-initiated photooxidation of smoke
551 extracts led to an increase in OP^{DTT} during the first 1 h. Upon prolonged photoaging,
552 the OP^{DTT} value decreased to $0.15 \mu\text{M DTT min}^{-1}$ after 23 h, slightly lower than the
553 corresponding initial values. Previous research results also suggested that aqueous OH
554 oxidation of WS-BBOA components generally leads to a final reduction in OP^{DTT}
555 (Wong et al., 2019; Jiang and Jang, 2018) during prolong irradiation, consistent to our
556 findings. The temporal variation pattern of OP^{DTT} is comparable to that observed for
557 aqueous oxidation of soybean straw extracts (Ye et al., 2025), but opposite to that of
558 4NC photodegradation (Lei et al., 2025). The DTT activity is likely associated with
559 light-absorbing and fluorescent substances containing large conjugated electron
560 systems, which can transfer electrons to participate in catalytic reaction, thereby
561 contributing to DTT activity (Chen et al., 2019). The reduction in DTT activity after
562 23 h agrees with the decrease of lignin-like and aromatic compounds revealed by
563 FT-ICR MS analysis.

564 Given that aqueous OH oxidation did not significantly reduce the total WSOC
565 concentrations, the decrease in OP^{DTT} is likely attributed to the formation of non- or
566 less DTT-active components. However, total WSOC decreased significantly upon



567 aging; consequently, the OP^{DTT} normalized by WSOC increased over irradiation time,
568 suggesting the possible formation of secondary toxic organic species during the aging
569 processes. Previous published studies have also showed that photochemical aging of
570 fresh particles can either enhance or diminish toxicity, depending on their sources and
571 oxidation conditions (Fang et al., 2024). To further characterize the ROS-generation
572 potential of WSOM from different combustion sources, we calculated the
573 WSOC-normalized DTT consumption rate (OP_{WSOC}^{DTT} , OP^{DTT} divided by WSOC). The
574 results showed that the mass-normalized DTT consumption rates gradually increased
575 and reached a plateau at 132 and 82 pmol/min/ μg for maize and coal smoke extracts,
576 respectively, similar to finding from Wong et al. (2019). These values are higher than
577 those reported for water extracts from $PM_{2.5}$ aerosol (22-68 pmol·min⁻¹· μg^{-1}) (Verma et
578 al., 2012). Based on the molecular-level differences after $\bullet\text{OH}$ photooxidation, the
579 reasons for the OP_{WSOC}^{DTT} changes induced by OH-photolysis in coal and maize are
580 likely different. For coal, the increase in OP_{WSOC}^{DTT} may primarily result from the
581 formation of CHON compounds after photolysis, whereas for maize, the increase is
582 probably due to the production of more quinone species or OH addition products
583 during the reaction (Tang et al., 2025; Wong et al., 2019).

584 Unfortunately, due to the limitations of current analytical techniques, it remains
585 challenging or even impossible to attribute the observed DTT variation trends to
586 specific molecular species.



587

588 **Fig. 9.** (a) Temporal evolution of DTT consumption rate and (b) WSOC-normalized DTT activity

589 for both smoke extracts during aqueous OH photooxidation.

590 3.6 ROS contribution and Reaction mechanism

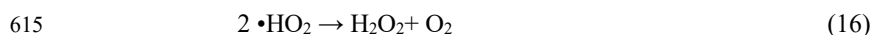
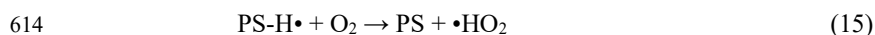
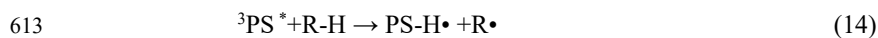
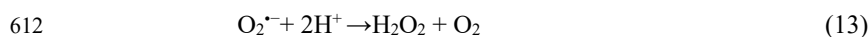
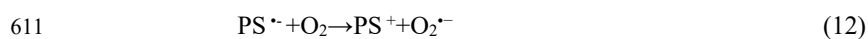
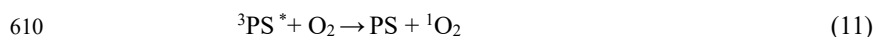
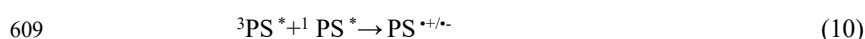
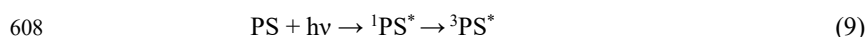
591 3.6.1 ROS concentration and relative contribution

592 Hydrogen peroxide can undergo photolysis to generate $\cdot OH$, which effectively
593 break down chromophores, thereby decreasing light absorption. The OH radicals can
594 oxidize most organic species, leading to a sharp decrease in both WSOC and
595 absorbance during the initial reaction stage.

596 According to previous studies (Arciva et al., 2022), when the concentration of the
597 BB mixture reaches 12 mg C/L, the concentration of photosensitizers in solution can
598 exceed several millimoles. This suggests that the smoke samples in the present study
599 likely contains substantial amounts of photosensitizing compounds. Upon exposure to
600 sunlight, these photosensitizer (denoted as PS) absorb photons and transition to their
601 triplet excited state ($^3PS^*$). The excited triplet states can subsequently react with O_2 to
602 produce various ROS, including 1O_2 , superoxide ($O_2^{\cdot -}$), hydroperoxyl radical ($\cdot HO_2$),
603 and $\cdot OH$, through H-abstracting, electron transfer and energy transfer processes.



604 These ROS species actively participate in subsequent photooxidation reactions.



616 According to method described in Sect. 2.5, the steady-state concentrations of
617 $\cdot\text{OH}$ (denoted as $[\cdot\text{OH}]_{\text{ss}}$) and ${}^1\text{O}_2$ (denoted as $[{}^1\text{O}_2]_{\text{ss}}$) were determined using
618 electron paramagnetic resonance (EPR) based on their characteristic spectra.
619 5,5-Dimethyl-1-pyrroline N-oxide (DMPO) and 2,2,6,6-tetramethylpiperidine (TEMP)
620 were selected as spin-trapping agents for $\cdot\text{OH}$ and ${}^1\text{O}_2$ respectively (Hu et al., 2025).
621 The distinct 1:1:1 triplet EPR signal characteristic of ${}^1\text{O}_2$ and 1:2:2:1 quartet signal of
622 $\cdot\text{OH}$ confirmed the generation of ${}^1\text{O}_2$ and $\cdot\text{OH}$, with signal intensities increasing as the
623 reaction time progressed. (Fig. S10). Moreover, a chemical probe method was
624 employed to further quantify the concentrations of $\cdot\text{OH}$ and ${}^1\text{O}_2$. Benzoic acid (BA)
625 was used as the $\cdot\text{OH}$ probe compound according to previously established protocol
626 (Hu et al., 2025). Briefly, six different concentration of BA (5, 10, 15, 20, 30, 40 and
627 50 μM) were added to separate aliquots of the same extract. After illuminating for



628 time t , the residual BA concentration was monitored by UPLC-PDA. A linear
629 regression of $-\ln[\text{BA}]/\ln[\text{BA}]_0$ versus reaction time t yielded the pseudo-first-order
630 rate constant (k_{BA}) (Fig. 10 a, b). By plotting the reciprocal ($1/k_{\text{BA}}$) against $[\text{BA}]$, the
631 intercept was obtained (Fig. 10 c), from which $[\text{OH}]_{\text{ss}}$, was determined by dividing the
632 intercept by the second-order rate constants $k_{\text{BA, OH}}$ ($5.1 \times 10^9 \text{ M}^{-1} \text{ s}^{-1}$) (Lei et al., 2023).
633 The estimated $[\text{OH}]_{\text{ss}}$ were $9.11 \times 10^{-14} \text{ M}$ and $8.58 \times 10^{-14} \text{ M}$ for coal and maize smoke
634 extracts, respectively (Fig. 10)—values comparable to those typically observed in
635 atmospheric cloud droplets (Arakaki et al., 2013; Li et al., 2023).

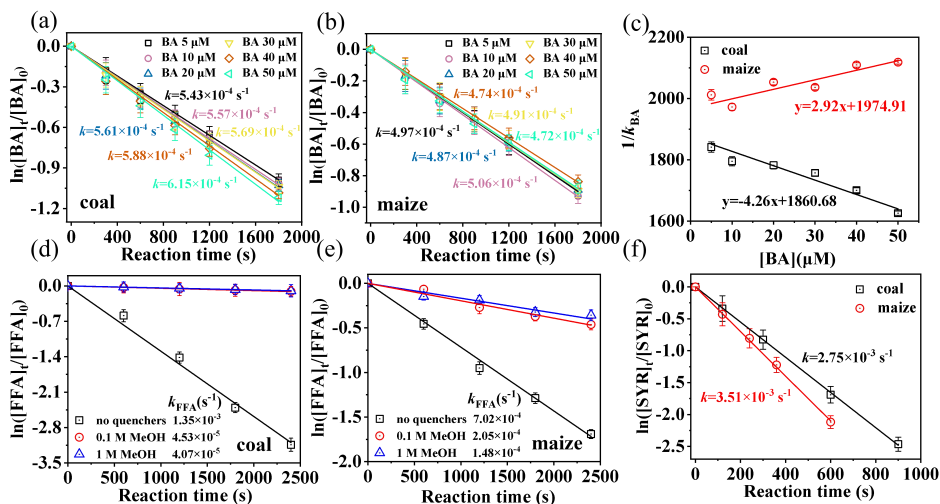
636 The steady-state concentrations of $^1\text{O}_2$ and $^3\text{C}^*$ were also quantified by
637 monitoring the decay of furfuryl alcohol (FFA) and syringol (SYR) under
638 pseudo-first-order kinetics (Fig. 10d-f), following previously established procedures
639 (Li et al., 2024). Considering the relatively high $\bullet\text{OH}$ concentration in the mixed
640 system, potential interference may occur when using FFA as a probe, since it can react
641 with both $\bullet\text{OH}$ ($k_{\text{FFA, OH}}=1.5 \times 10^{10} \text{ M}^{-1} \text{ s}^{-1}$) and $^1\text{O}_2$ ($k_{\text{FFA, }^1\text{O}_2}=1.2 \times 10^8 \text{ M}^{-1} \text{ s}^{-1}$). To
642 eliminate this interference, excess methanol was added to completely quench $\bullet\text{OH}$
643 ($k_{\text{MeOH, OH}}=1.0 \times 10^9 \text{ M}^{-1} \text{ s}^{-1}$) before employing FFA to determine the $^1\text{O}_2$ concentration.
644 The results (Fig. 10) showed that the $[\text{O}_2]_{\text{ss}}$ values were $3.48 \times 10^{-13} \text{ M}$ and 1.8×10^{-12}
645 M for coal and maize smoke extracts, respectively, higher than that reported for 5
646 mgC L^{-1} of SOA extracts ($3 \times 10^{-14} \text{ M}$) (Manfrin et al., 2019). Generally, $^1\text{O}_2$ was born
647 by triplets thus tightly linked to $^3\text{C}^*$. The significantly higher $^1\text{O}_2$ concentration
648 observed in maize smoke extracts—approximately six times that of coal smoke
649 extracts—indicates a greater abundance of triplet-state precursors in maize-derived
650 WSOM. Similarly, SYR was employed as a chemical probe due to its high reactivity



651 with triplets ($k_{\text{SYR},3\text{C}^*}=3.9 \times 10^9 \text{ M}^{-1} \text{ s}^{-1}$) (Ma et al., 2023). Based on its
652 pseudo-first-order decay kinetics, the steady-state concentrations of $^3\text{C}^*$ in the maize
653 and coal systems were determined to be $9.0 \times 10^{-13} \text{ M}$ and $7.05 \times 10^{-13} \text{ M}$, respectively
654 (Fig. 11f).

655 The steady-state concentrations determined in our system are approximately one
656 order of magnitude higher than those reported in aqueous PM extracts illuminated
657 with 365 nm lamps (e.g., $\sim 10^{-13} \text{ M}$ for triplets) (Bogler et al., 2022). Data from Ma et
658 al. (2024) also showed the concentrations of $\bullet\text{OH}$, $^1\text{O}_2$, and $^3\text{C}^*$ in $\text{PM}_{2.5}$ extracts range
659 from $(0.2\text{--}4.7) \times 10^{-15} \text{ M}$, $(0.7\text{--}45) \times 10^{-13} \text{ M}$, and $(0.03\text{--}7.9) \times 10^{-13} \text{ M}$, respectively.
660 This significant difference is mainly attributed to the addition of 10 mM H_2O_2 in our
661 experiments. Given an estimated average molecular weight of 300 g/mol for WSOM,
662 the resulting molar ratio of H_2O_2 to WSOM (15 mg C/L) is approximately 200:1. This
663 substantial excess of H_2O_2 provides a high concentration of $\bullet\text{OH}$, sufficient to
664 extensively oxidize WSOM and explaining why our $\bullet\text{OH}$ levels are orders of
665 magnitude greater than those in typical PM extracts (Ma et al., 2024).

666 Consequently, the degradation of WSOM in our system is predominantly driven
667 by $\bullet\text{OH}$ oxidation, with minor contributions from other reactive species. Furthermore,
668 the concentrations of $^1\text{O}_2$ and $^3\text{C}^*$ were also slightly higher than those in ambient PM
669 extracts (Ma et al., 2024), likely because our simulated combustion samples contained
670 higher levels of phenolic compounds and PAHs, which are known precursors for these
671 species.



672

673 **Fig. 10.** Loss of (a,b) BA, (d,e) FFA, (f) SYR and (c) plot of $1/k_{BA}$ and BA concentration

674 To elucidate the reaction mechanism, the role of different ROS in the photodecay
 675 and light absorbance of smoke extracts were examined. The absorption spectra of
 676 smoke extracts with and without 0.1 M methanol ($\cdot\text{OH}$ quencher) were compared (Fig.
 677 S11). A molar ratio of 2000:1 (MeOH: WSOM) was employed, assuming an average
 678 molecular weight of 300 g/mol, to ensure complete scavenging OH given the
 679 comparable second-order rate constants of MeOH and WSOM with $\cdot\text{OH}$ (Liu-Kang et
 680 al., 2024). As shown in Fig. S11, absorbance decay rate decreased markedly,
 681 especially within the first hour, indicating that $\cdot\text{OH}$ play a dominant role in the
 682 photodecay of the extracts.

683 To further assess the contributions of individual ROS, comparative experiments
 684 were conducted under N_2 -, air-, and O_2 -saturated conditions. Under N_2 saturation,
 685 secondary oxidants such as $\text{HO}_2\cdot$ and $\cdot\text{OH}$ were largely excluded due to the absence
 686 of oxygen. The changes in WSOC indicate that direct photolysis in both smoke



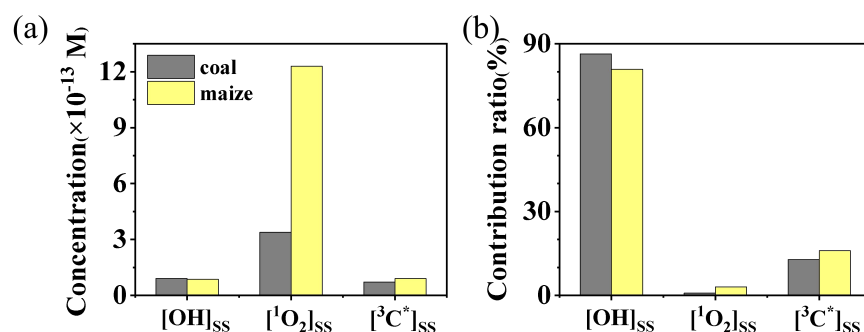
687 extracts was much weaker than $\bullet\text{OH}$ oxidation. Under $\bullet\text{OH}$ oxidation, the WSOC
688 loss under N_2 -saturated conditions was much lower than that under O_2 - and
689 air-saturated conditions (Fig. S12), whereas in direct photolysis, the differences
690 among the three gas conditions were negligible (Fig. S13). This suggests that O_2 plays
691 a crucial role only for $\bullet\text{OH}$ oxidation.

692 Previous studies have reported that $^3\text{C}^*$ -initiated photooxidation of phenolic
693 compounds proceeds most rapidly under N_2 -saturated conditions (Lei et al., 2023). In
694 contrast, our results showed the fastest degradation under O_2 -saturated and the slowest
695 under N_2 , implying that $^3\text{C}^*$ is not the dominant oxidant in our system. This
696 conclusion is further supported by the comparable WSOC degradation observed for
697 coal and maize smoke extracts. Theoretically, if $^3\text{C}^*$ were the primary oxidant, maize
698 extracts would be expected to exhibit a much higher WSOC degradation owing to
699 their greater content of photosensitizers, as indicated by the higher lignin-like
700 compounds in maize (Sec. 3.3).

701 The relative importance of individual ROS in WSOM photodecay was evaluated
702 by multiplying their corresponding second-order rate constants with their steady-state
703 concentrations. Thus, we estimated the relative role in smoke WSOM photodecay.
704 Given that reaction rates of WSOC with $\bullet\text{OH}$ and $^3\text{C}^*$ were $3.8 \times 10^8 \text{ M}^{-1}\text{s}^{-1}$ and
705 $7.2 \times 10^7 \text{ M}^{-1}\text{s}^{-1}$, whereas $^1\text{O}_2$ reacts much more slowly ($10^5 \text{ M}^{-1}\text{s}^{-1}$) (Ma et al., 2024),
706 the contributions were calculated (Fig. 10b). For coal smoke extract, $\bullet\text{OH}$, $^3\text{C}^*$, $^1\text{O}_2$
707 accounted for approximate 86.4%, 12.8% and 0.8% of the total oxidation, respectively.
708 A similar pattern was observed for maize smoke extracts (80.9%, 16.0% and 3.1%),



709 with the overall contribution order of $\cdot\text{OH} > {}^3\text{C}^* > {}^1\text{O}_2$. Although ${}^1\text{O}_2$ exhibited the
710 highest steady-state concentration, its low reactivity limited its overall contribution,
711 consistent with previous findings (Zhang et al., 2024). According to earlier reports
712 (Tang et al., 2025), when the concentration of the BB-derived mixture reaches 12 mg
713 C/L, the concentration of photosensitizers in solution can exceed several millimoles.
714 Therefore, ${}^3\text{C}^*$ also plays an important and non-negligible role in the
715 photodegradation of both smoke WSOM.



716

717 **Fig. 11.** ROS steady-state contribution and their contribution to WSOM photodecay

718 3.6.2 Photochemical transformation of smoke extracts

719 By introducing extra H_2O_2 , the $\cdot\text{OH}$ concentration and its role in the photoaging
720 of both smoke extracts were altered. The added $\cdot\text{OH}$ accounts for a major fraction of
721 the total oxidants in both systems, thereby influencing the overall optical properties
722 and chemical composition. Based on the ROS measurements and molecular analyses,
723 a conceptual mechanism for the aqueous photooxidation of both smoke extracts is
724 proposed (Fig. 12). Upon irradiation, photosensitizers in WSOM absorb photons and
725 form triplet excited states (${}^3\text{PS}^*$), which transfer energy or electrons to dissolved O_2 ,
726 generating various ROS (${}^1\text{O}_2$, O_2^- , $\cdot\text{HO}_2$, and $\cdot\text{OH}$). These reactive species initiate and



727 propagate oxidation processes, thereby modifying the chemical composition and
728 optical properties of WSOM.

729 In the first stage, abundant $\bullet\text{OH}$ rapidly attacks electron-rich aromatic and
730 conjugated structures, cleaving C=C and C–O bonds and causing a sharp decrease in
731 WSOC and light absorbance. Meanwhile, both $^3\text{Sen}^*$ and $^1\text{O}_2$ selectively oxidizes
732 lignin-like compounds, forming oxygenated intermediates such as carbonyls, and
733 carboxylic acids, resulting in gradual decrease in solution pH (Fig. S7) and increase in
734 O/C.

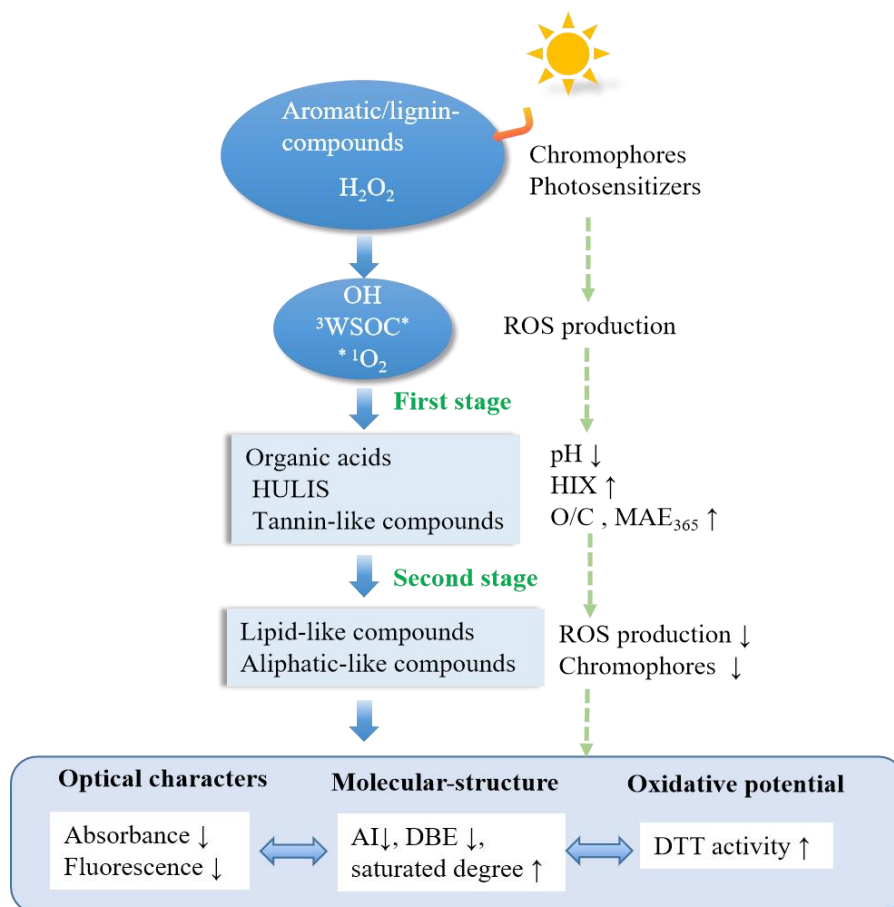
735 As the reaction proceeds, the depletion of aromatic chromophores suppresses
736 further ROS formation, consistent with the observed decline in DTT activity. FT-ICR
737 MS analysis further supports this evolution, revealing a shift from high H/C, low O/C
738 aromatic compounds toward lipid- or aliphatic-like species.

739 Interestingly, although total WSOC decreased with aging, WSOC-normalized
740 DTT activity increased due to probable highly DTT active species (e.g., quinone-like
741 species). Similar trends have been observed in BBOA-WSOC OH-photooxidation
742 aging, where oxidative potential decreased at the initial period (~ 5 h) despite WSOC
743 mass loss (Wong et al., 2019).

744 Overall, the aqueous photooxidation of combustion-emitted smoke extracts
745 involves a dynamic interplay among $\bullet\text{OH}$, $^3\text{C}^*$, and $^1\text{O}_2$. The early stage is dominated
746 by $\bullet\text{OH}$ -driven degradation of chromophores, followed by secondary formation of
747 oxygenated, potentially more toxic species through $^1\text{O}_2$ and triplet-state reactions.
748 These processes jointly govern the chemical evolution, light-absorbing behavior, and



749 oxidative potential of WSOM during photochemical aging.



750

751 **Fig. 12.** Proposed photochemical transformation pathway for two smoke extracts

752

753 4 Conclusions

754 This study systematically investigated the aqueous-phase •OH photodegradation
 755 of coal- and maize-derived smoke extracts, providing mechanistic insights into their
 756 molecular and optical transformations. EEM-PARAFAC identified one humic-like
 757 and two protein-like components, revealing distinct temporal patterns for coal and
 758 maize smoke extracts. FT-ICR MS characterization showed that CHO and CHON



759 compounds dominated both samples, with maize smoke exhibiting higher CHON
760 content and coal smoke enriched in sulfur-containing species. Aqueous $\bullet\text{OH}$
761 photooxidation increased molecular saturation and reduced aromaticity, as reflected
762 by lower DBE and AI values. Lignin-like compounds declined, whereas lipid- and
763 aliphatic-like fractions increased, indicating transformation of aromatic species into
764 more saturated, water-soluble products.

765 Distinct photodegradation pathways were observed for coal and maize extracts.
766 The contributions of ROS to photodegradation followed the order $\bullet\text{OH} > {}^3\text{C}^* > {}^1\text{O}_2$,
767 highlighting the dominant role of OH radical in aqueous-phase transformations.
768 Early-stage formation of carboxylic acids, evidenced by increased oxalate, CHO_2^+
769 fragments, and declining pH, was confirmed by HR-AMS, which also revealed
770 enhanced oxidation of aqSOA, particularly in maize smoke extracts. Although total
771 WSOC decreased during photodegradation, the WSOC-normalized oxidative potential
772 increased, as indicated by enhanced DTT consumption, likely due to the formation of
773 nitrogen-containing compounds in coal smoke and reactive quinones in maize smoke.

774 Overall, aqueous photochemical processing simultaneously decreases light
775 absorption and fluorescence while enhancing oxidative potential. Maize smoke
776 aqSOA exhibited higher oxidation degrees than coal, whereas coal smoke generated a
777 higher aqSOA mass yield. The observed molecular evolution and photochemical
778 reactivity indicate that water-soluble products from biomass and coal combustion
779 undergo distinct pathways during atmospheric aging.

780 These findings suggest that aqueous-phase photochemistry can significantly alter
781 the optical and chemical properties of smoke-derived WSOM during cloud and fog
782 processing. The transformation of aromatic chromophores into more saturated and
783 aliphatic products reduces brown carbon light absorption, potentially weakening the



784 direct radiative forcing of biomass and coal emissions. Simultaneously, the formation
785 of highly oxidized products, including quinones and nitrogen-containing compounds,
786 enhances oxidative potential and may increase the toxicity of aged aerosols,
787 influencing cloud chemistry, secondary organic aerosol formation, and heterogeneous
788 reactions in the atmosphere. Incorporating these aqueous-phase transformations into
789 atmospheric models is therefore essential to more accurately assess the climate and air
790 quality impacts of smoke emissions from different fuel sources.

791 **Author contributions.**

792 ZY and XG developed the research objectives and designed the experiments. DH
793 and XH set up the combustion sampling apparatus and collected samples. DH and QC
794 conducted the photochemistry experiments and analyzed the data with the help of XH.
795 ZY prepared the manuscript with contributions from all co-authors. ZY and XG
796 provided supervision and guidance during the experiments and writing.

797 **Acknowledgements.**

798 The authors acknowledge support from the Natural Science Foundation of
799 Jiangsu Province (BK20221405) and National foreign expert project (H20240368).
800 We are also thankful for funding support from Natural Science Foundation of China
801 (22361162668), Natural Science Foundation of the Jiangsu Higher Education
802 Institutions of China (25KJD170010), and the Postgraduate Research & Practice
803 Innovation Program of Jiangsu Province (SJCX24_1808). We also thank for the
804 support from the Jiangsu Key Laboratory of Electronic Waste and New Energy Solid
805 Waste Resources Utilization.

806 **References**



- 807 Arakaki, T., Anastasio, C., Kuroki, Y., Nakajima, H., Okada, K., Kotani, Y., Handa, D., Azechi,
808 S., Kimura, T., Tsuchioka, A., and Miyagi, Y.: A general scavenging rate constant for reaction of
809 hydroxyl radical with organic carbon in atmospheric waters, *Environ. Sci. Technol.*, 47,
810 8196–8203, <https://doi.org/10.1021/es401927b>, 2013.
- 811 Arciva, S., Niedek, C., Mavis, C., Yoon, M., Sanchez, M. E., Zhang, Q., and Anastasio, C.:
812 Aqueous ·OH oxidation of highly substituted phenols as a source of secondary organic aerosol,
813 *Environ. Sci. Technol.*, 56, 9959–9967, <https://doi.org/10.1021/acs.est.2c02225>, 2022.
- 814 Arciva, S., Ma, L., Mavis, C., Guzman, C., and Anastasio, C.: Formation and loss of light
815 absorbance by phenolic aqueous SOA by OH and an organic triplet excited state, *Atmos. Chem.*
816 *Phys.*, 24, 4473–4485, <https://doi.org/10.5194/acp-24-4473-2024>, 2024.
- 817 Bogler, S., Daellenbach, K. R., Bell, D. M., Prévôt, A. S. H., El Haddad, I., and
818 Borduas-Dedekind, N.: Singlet oxygen seasonality in aqueous PM₁₀ is driven by biomass
819 burning and anthropogenic secondary organic aerosol, *Environ. Sci. Technol.*, 56, 15389–15397,
820 <https://doi.org/10.1021/acs.est.2c04554>, 2022.
- 821 Cao, T., Xu, C., Chen, H., Song, J., Li, J., Song, H., Jiang, B., Zhong, Y., and Peng, P.: Molecular
822 insight into aqueous-phase photolysis and photooxidation of water-soluble organic matter
823 emitted from biomass burning and coal combustion, *Atmos. Chem. Phys.*, 25, 11597–11610,
824 <https://doi.org/10.5194/acp-25-11597-2025>, 2025.
- 825 Chen, Q., Wang, M., Wang, Y., Zhang, L., Li, Y., and Han, Y.: Oxidative potential of
826 water-soluble matter associated with chromophoric substances in PM_{2.5} over Xi'an, China,
827 *Environ. Sci. Technol.*, 53, 8574–8584, <https://doi.org/10.1021/acs.est.9b01976>, 2019.



- 828 Chen, W., Zhang, H., Xu, S., Jia, H., Qi, Z., Farooq, U., Wang, Z., and Dai, Q.: New insights into
829 the molecular characteristics-dependent light absorption variation of water-soluble organic
830 matter in biomass burning smoke, *Atmos. Res.*, 316, 107951,
831 <https://doi.org/10.1016/j.atmosres.2025.107951>, 2025.
- 832 Cook, R. D., Lin, Y.-H., Peng, Z., Boone, E., Chu, R. K., Dukett, J. E., Gunsch, M. J., Zhang, W.,
833 Tolic, N., Laskin, A., and Pratt, K. A.: Biogenic, urban, and wildfire influences on the
834 molecular composition of dissolved organic compounds in cloud water, *Atmos. Chem. Phys.*,
835 17, 15167–15180, <https://doi.org/10.5194/acp-17-15167-2017>, 2017.
- 836 Fan, X., Wei, S., Zhu, M., Song, J., and Peng, P.: Comprehensive characterization of humic-like
837 substances in smoke PM_{2.5} emitted from the combustion of biomass materials and fossil fuels,
838 *Atmos. Chem. Phys.*, 16, 13321–13340, <https://doi.org/10.5194/acp-16-13321-2016>, 2016.
- 839 Fan, X., Li, M., Cao, T., Cheng, C., Li, F., Xie, Y., Wei, S., Song, J., and Peng, P.: Optical
840 properties and oxidative potential of water- and alkaline-soluble brown carbon in smoke
841 particles emitted from laboratory simulated biomass burning, *Atmos. Environ.*, 194, 48–57,
842 <https://doi.org/10.1016/j.atmosenv.2018.09.025>, 2018.
- 843 Fan, X., Xie, S., Yu, X., Cheng, A., Chen, D., Ji, W., Liu, X., Song, J., and Peng, P.:
844 Molecular-level transformations of biomass burning-derived water-soluble organic carbon
845 during dark aqueous OH oxidation: Insights from absorption, fluorescence, high-performance
846 size exclusion chromatography and high-resolution mass spectrometry analysis, *Sci. Total*
847 *Environ.*, 912, 169290, <https://doi.org/10.1016/j.scitotenv.2023.169290>, 2024.
- 848 Fang, Z., Lai, A., Cai, D., Li, C., Carmieli, R., Chen, J., Wang, X., and Rudich, Y.: Secondary
849 organic aerosol generated from biomass burning emitted phenolic compounds: Oxidative



850 potential, reactive oxygen species, and cytotoxicity, *Environ. Sci. Technol.*, 58, 8194–8206,
851 <https://doi.org/10.1021/acs.est.3c09903>, 2024.

852 Gerritz, L., Wei, J., Fang, T., Wong, C., Klodt, A. L., Nizkorodov, S. A., and Shiraiwa, M.:
853 Reactive oxygen species formation and peroxide and carbonyl decomposition in aqueous
854 photolysis of secondary organic aerosols, *Environ. Sci. Technol.*, 58, 4716–4726,
855 <https://doi.org/10.1021/acs.est.3c08662>, 2024.

856 Go, B. R., Li, Y. J., Huang, D. D., Wang, Y., and Chan, C. K.: Comparison of aqueous secondary
857 organic aerosol (aqSOA) product distributions from guaiacol oxidation by non-phenolic and
858 phenolic methoxybenzaldehydes as photosensitizers in the absence and presence of ammonium
859 nitrate, *Atmos. Chem. Phys.*, 23, 2859–2875, <https://doi.org/10.5194/acp-23-2859-2023>, 2023.

860 Go, B. R., Li, Y. J., Huang, D. D., and Chan, C. K.: Aqueous-phase photoreactions of mixed
861 aromatic carbonyl photosensitizers yield more oxygenated, oxidized, and less light-absorbing
862 secondary organic aerosol (SOA) than single systems, *Environ. Sci. Technol.*, 58, 7924–7936,
863 <https://doi.org/10.1021/acs.est.3c10199>, 2024.

864 Hems, R. F., Schnitzler, E. G., Bastawrous, M., Soong, R., Simpson, A. J., and Abbatt, J. P. D.:
865 Aqueous photoreactions of wood smoke brown carbon, *ACS Earth Space Chem.*, 4, 1149–1160,
866 <https://doi.org/10.1021/acsearthspacechem.0c00117>, 2020.

867 Hu, D., Ye, Z., Wang, Z., Topping, D., Aruffo, E., Wang, H., and Ge, X.: Kinetics and quantum
868 yield of photosensitized reactions from substituted phenols via chemical probe approach, *Atmos.*
869 *Environ.*, 360, 121419, <https://doi.org/10.1016/j.atmosenv.2025.121419>, 2025a.



- 870 Hu, D., Wang, Z., Aruffo, E., Dai, X., Zhao, Z., and Ye, Z.: Kinetics of different substituted
871 Phenolic compounds' aqueous OH oxidation in atmosphere, *Atmosphere*, 16,
872 <https://doi.org/10.3390/atmos16050567>, 2025b.
- 873 Huang, Y., Li, X., Huang, D. D., Lei, R., Zhou, B., Zhang, Y., and Ge, X.:
874 Machine-learning-assisted chemical characterization and optical properties of atmospheric
875 brown carbon in Nanjing, China, *Atmos. Chem. Phys.*, 25, 7619–7645,
876 <https://doi.org/10.5194/acp-25-7619-2025>, 2025.
- 877 Jiang, H. and Jang, M.: Dynamic oxidative potential of atmospheric organic aerosol under ambient
878 sunlight, *Environ. Sci. Technol.*, 52, 7496–7504, <https://doi.org/10.1021/acs.est.8b00148>, 2018.
- 879 Jiang, W., Misovich, M. V., Hettiyadura, A. P. S., Laskin, A., McFall, A. S., Anastasio, C., and
880 Zhang, Q.: Photosensitized reactions of a phenolic carbonyl from wood combustion in the
881 aqueous phase—Chemical evolution and light absorption properties of aqSOA, *Environ. Sci.*
882 *Technol.*, <https://doi.org/10.1021/acs.est.0c07581>, 2021.
- 883 Jiang, W., Niedek, C., Anastasio, C., and Zhang, Q.: Photoaging of phenolic secondary organic
884 aerosol in the aqueous phase: evolution of chemical and optical properties and effects of
885 oxidants, *Atmos. Chem. Phys.*, 23, 7103–7120, <https://doi.org/10.5194/acp-23-7103-2023>,
886 2023.
- 887 Lei, R., Sha, Y., Meng, H., Huang, Y., Ye, J., Huang, D. D., Zhang, Y., Wu, Y., Li, Y., and Ge, X.:
888 Aqueous phase photolysis of 4-nitrocatechol: Reaction kinetics, evolutions of chemical
889 composition, light absorption and oxidation potential, *Atmos. Environ.*, 343, 120981,
890 <https://doi.org/10.1016/j.atmosenv.2024.120981>, 2025.



- 891 Lei, Y., Yu, Y., Lei, X., Liang, X., Cheng, S., Ouyang, G., and Yang, X.: Assessing the use of
892 probes and quenchers for understanding the reactive species in advanced oxidation processes,
893 Environ. Sci. Technol., 57, 5433–5444, <https://doi.org/10.1021/acs.est.2c09338>, 2023.
- 894 Lei, Y., Lei, X., Tian, G., Yang, J., Huang, D., Yang, X., Chen, C., and Zhao, J.: Optical variation
895 and molecular transformation of brown carbon during oxidation by NO₃• in the aqueous phase,
896 Environ. Sci. Technol., 58, 3353–3362, <https://doi.org/10.1021/acs.est.3c08726>, 2024.
- 897 Leresche, F., Salazar, J. R., Pfothhauer, D. J., Hannigan, M. P., Majestic, B. J., and Rosario-Ortiz,
898 F. L.: Photochemical aging of atmospheric particulate matter in the aqueous phase, Environ. Sci.
899 Technol., 55, 13152–13163, <https://doi.org/10.1021/acs.est.1c00978>, 2021.
- 900 Li, F., Tsona, N. T., Li, J., and Du, L.: Aqueous-phase oxidation of syringic acid emitted from
901 biomass burning: Formation of light-absorbing compounds, Sci. Total Environ., 765, 144239,
902 <https://doi.org/10.1016/j.scitotenv.2020.144239>, 2021.
- 903 Li, F., Zhou, S., Du, L., Zhao, J., Hang, J., and Wang, X.: Aqueous-phase chemistry of
904 atmospheric phenolic compounds: A critical review of laboratory studies, Sci. Total Environ.,
905 856, 158895, <https://doi.org/10.1016/j.scitotenv.2022.158895>, 2023.
- 906 Li, F., Zhou, S., Zhao, J., Hang, J., Lu, H., Li, X., Gao, M., Li, Y., and Wang, X.: Aqueous
907 photosensitization of syringaldehyde: Reactivity, effects of environmental factors, and
908 formation of brown carbon products, ACS Earth Space Chem., 8, 1193–1203,
909 <https://doi.org/10.1021/acsearthspacechem.4c00004>, 2024a.
- 910 Li, L., Han, Y., Li, J., Lin, Y., Zhang, X., Wang, Q., and Cao, J.: Effects of photochemical aging
911 on the molecular composition of organic aerosols derived from agricultural biomass burning in



- 912 whole combustion process, *Sci. Total Environ.*, 946, 174152,
913 <https://doi.org/10.1016/j.scitotenv.2024.174152>, 2024b.
- 914 Li, X., Tao, Y., Zhu, L., Ma, S., Luo, S., Zhao, Z., Sun, N., Ge, X., and Ye, Z.: Optical and
915 chemical properties and oxidative potential of aqueous-phase products from OH and
916 $^3\text{C}^*$ -initiated photooxidation of eugenol, *Atmos. Chem. Phys.*, 22, 7793–7814,
917 <https://doi.org/10.5194/acp-22-7793-2022>, 2022.
- 918 Liu-Kang, C., Sokolova, A., Gong, Y., Fahy, W. D., Peng, H., and Abbatt, J. P. D.: Light exposure
919 of wood smoke aerosol: Connecting optical properties, oxidation, radical formation, and
920 chemical composition, *ACS EST Air*, 1, 273–282, <https://doi.org/10.1021/acsestair.3c00063>,
921 2024.
- 922 Ma, L., Worland, R., Jiang, W., Niedek, C., Guzman, C., Bein, K. J., Zhang, Q., and Anastasio, C.:
923 Predicting photooxidant concentrations in aerosol liquid water based on laboratory extracts of
924 ambient particles, *Atmos. Chem. Phys.*, 23, 8805–8821,
925 <https://doi.org/10.5194/acp-23-8805-2023>, 2023.
- 926 Ma, L., Worland, R., Heinlein, L., Guzman, C., Jiang, W., Niedek, C., Bein, K. J., Zhang, Q., and
927 Anastasio, C.: Seasonal variations in photooxidant formation and light absorption in aqueous
928 extracts of ambient particles, *Atmos. Chem. Phys.*, 24, 1–21,
929 <https://doi.org/10.5194/acp-24-1-2024>, 2024.
- 930 Mahamuni, G., Rutherford, J., Davis, J., Molnar, E., Posner, J. D., Seto, E., Korshin, G., and
931 Novosselov, I.: Excitation–emission matrix spectroscopy for analysis of chemical composition
932 of combustion generated particulate matter, *Environ. Sci. Technol.*, 54, 8198–8209,
933 <https://doi.org/10.1021/acs.est.0c01110>, 2020.



- 934 Manfrin, A., Nizkorodov, S. A., Malecha, K. T., Getzinger, G. J., McNeill, K., and
935 Borduas-Dedekind, N.: Reactive oxygen species production from secondary organic aerosols:
936 The importance of singlet oxygen, *Environ. Sci. Technol.*, **53**, 8553–8562,
937 <https://doi.org/10.1021/acs.est.9b01609>, 2019.
- 938 Ning, C., Tang, Y., Sun, S., Wang, D., and Gao, Y.: Molecular level characteristics and sources of
939 rainwater water-soluble organic matter in different regions of China by FT-ICR MS, *Atmos.*
940 *Environ.*, **350**, 121175, <https://doi.org/10.1016/j.atmosenv.2025.121175>, 2025.
- 941 Song, J., Li, M., Jiang, B., Wei, S., Fan, X., and Peng, P.: Molecular characterization of
942 water-soluble humic like substances in smoke particles emitted from combustion of biomass
943 materials and coal using ultrahigh-resolution electrospray ionization Fourier Transform Ion
944 Cyclotron Resonance Mass Spectrometry, *Environ. Sci. Technol.*, **52**, 2575–2585,
945 <https://doi.org/10.1021/acs.est.7b06126>, 2018.
- 946 Tang, J., Li, J., Su, T., Han, Y., Mo, Y., Jiang, H., Cui, M., Jiang, B., Chen, Y., Tang, J., Song, J.,
947 Peng, P., and Zhang, G.: Molecular compositions and optical properties of dissolved brown
948 carbon in biomass burning, coal combustion, and vehicle emission aerosols illuminated by
949 excitation–emission matrix spectroscopy and Fourier transform ion cyclotron resonance mass
950 spectrometry analysis, *Atmos. Chem. Phys.*, **20**, 2513–2532,
951 <https://doi.org/10.5194/acp-20-2513-2020>, 2020.
- 952 Tang, R., Ma, J., Zhang, R., Cui, W., Qin, Y., Chu, Y., Qin, Y., Vogel, A. L., and Chan, C. K.:
953 Enhanced sulfate formation in mixed biomass burning and sea-salt interactions mediated by
954 photosensitization: effects of chloride, nitrogen-containing compounds, and atmospheric aging,
955 *Atmos. Chem. Phys.*, **25**, 425–439, <https://doi.org/10.5194/acp-25-425-2025>, 2025.



- 956 Tomaz, S., Cui, T., Chen, Y., Sexton, K. G., Roberts, J. M., Warneke, C., Yokelson, R. J., Surratt,
957 J. D., and Turpin, B. J.: Photochemical cloud processing of primary wildfire emissions as a
958 potential source of secondary organic aerosol, *Environ. Sci. Technol.*, 52, 11027–11037,
959 <https://doi.org/10.1021/acs.est.8b03293>, 2018.
- 960 Verma, V., Rico-Martinez, R., Kotra, N., King, L., Liu, J., Snell, T. W., and Weber, R. J.:
961 Contribution of water-soluble and insoluble components and their hydrophobic/hydrophilic
962 subfractions to the reactive oxygen species-generating potential of fine ambient aerosols,
963 *Environ. Sci. Technol.*, 46, 11384–11392, <https://doi.org/10.1021/es302484r>, 2012.
- 964 Vione, D., Albinet, A., Barsotti, F., Mekic, M., Jiang, B., Minero, C., Brigante, M., and
965 Gligorovski, S.: Formation of substances with humic-like fluorescence properties, upon
966 photoinduced oligomerization of typical phenolic compounds emitted by biomass burning,
967 *Atmos. Environ.*, 206, 197–207, <https://doi.org/10.1016/j.atmosenv.2019.03.005>, 2019.
- 968 Wang, H., Zheng, N., Du, H., Chen, Z., Sha, H., Zhou, H., and Ye, Z.: Microheterogeneous
969 photogeneration of hydroxyl radical in sunlit dissolved black carbon solution, *J. Hazard. Mater.*,
970 498, 139840, <https://doi.org/10.1016/j.jhazmat.2025.139840>, 2025.
- 971 Wang, X., Hayeck, N., Brüggemann, M., Yao, L., Chen, H., Zhang, C., Emmelin, C., Chen, J.,
972 George, C., and Wang, L.: Chemical characteristics of organic aerosols in Shanghai: A study by
973 ultrahigh-performance liquid chromatography coupled with orbitrap mass spectrometry, *J.*
974 *Geophys. Res. Atmos.*, 122, 11,703–11,722, <https://doi.org/10.1002/2017JD026930>, 2017.
- 975 Wong, J. P. S., Nenes, A., and Weber, R. J.: Changes in light absorptivity of molecular weight
976 separated brown carbon due to photolytic aging, *Environ. Sci. Technol.*, 51, 8414–8421,
977 <https://doi.org/10.1021/acs.est.7b01739>, 2017.



- 978 Wong, J. P. S., Tsagkaraki, M., Tsiotra, I., Mihalopoulos, N., Violaki, K., Kanakidou, M., Sciare,
979 J., Nenes, A., and Weber, R. J.: Effects of atmospheric processing on the oxidative potential of
980 biomass burning organic aerosols, *Environ. Sci. Technol.*, 53, 6747–6756,
981 <https://doi.org/10.1021/acs.est.9b01034>, 2019.
- 982 Wu, G., Fu, P., Ram, K., Song, J., Chen, Q., Kawamura, K., Wan, X., Kang, S., Wang, X., Laskin,
983 A., and Cong, Z.: Fluorescence characteristics of water-soluble organic carbon in atmospheric
984 aerosol, *Environ. Pollut.*, 268, 115906, <https://doi.org/10.1016/j.envpol.2020.115906>, 2021.
- 985 Yang, N., Wang, J., Jacob, D. J., Ye, J., Sheng, M., Niu, M., Qin, Y., Ge, X., Sun, Y., Wang, Z.,
986 Wang, Y., Wu, F., Liu, C.-Q., George, C., and Fu, P.: Aqueous production of sulfur-containing
987 aerosols from nitroaromatic compounds and SO₂ in wintertime urban haze, *Sci. Bull.*, 70,
988 1846–1855, <https://doi.org/10.1016/j.scib.2025.03.013>, 2025.
- 989 Ye, Z., Hu, D., Wang, Z., Wang, H., and Ge, X.: Aqueous photochemical aging of water-soluble
990 smoke particles from crop straws burning, *Atmos. Environ.*, 340, 120897,
991 <https://doi.org/10.1016/j.atmosenv.2024.120897>, 2025.
- 992 Zhang, H., Wu, L., Qian, W., Ni, J., Wei, R., Qi, Z., and Chen, W.: Spectral characteristics of
993 dissolved organic carbon derived from biomass-pyrogenic smoke (SDOC) in the aqueous
994 environment and its solubilization effect on hydrophobic organic pollutants, *Water Res.*, 203,
995 117515, <https://doi.org/10.1016/j.watres.2021.117515>, 2021.
- 996 Zhang, J., Shrivastava, M., Ma, L., Jiang, W., Anastasio, C., Zhang, Q., and Zelenyuk, A.:
997 Modeling novel aqueous particle and cloud chemistry processes of biomass burning phenols
998 and their potential to form secondary organic aerosols, *Environ. Sci. Technol.*, 58, 3776–3786,
999 <https://doi.org/10.1021/acs.est.3c07762>, 2024.